Int J Earth Sci (Geol Rundsch) (2017) 106:2817–2836
DOI 10.1007/s00531-017-1461-1

ORIGINAL PAPER

Tectonic evolution of kid metamorphic complex and the recognition of Najd fault system in South East Sinai, Egypt

Yasser M. Sultan[1] · Mohamed K. El-Shafei[2,3] · Mohamed O. Arnous[3]

Received: 21 December 2016 / Accepted: 8 February 2017 / Published online: 14 March 2017

Abstract A low-to medium-grade metamorphic belt of a volcano-sedimentary succession occurs in the eastern side of South Sinai as a part of the northernmost extension of the Arabian–Nubian Shield in Egypt. The belt is known as the Kid metamorphic complex. It is considered as one of the major belt among the other exposed metamorphic belts in South Sinai. Here, we detect and investigate the signature of the Najd Fault system in South Sinai based on detailed structural analysis in field and digital image processing. The enhanced satellite image and the geo-spatial distributions confirm that the Kid belt is essentially composed of nine Precambrian units. Field relations and geometrical analysis of the measured structural data revealed that the study area underwent four successive deformational phases (D_1–D_4). D_1 is an upright tight to isoclinal large-scale folds that caused few F_1 small-scale folds and a steeply dipping S_1 axial plane foliation. The second deformational event D_2 produced dominant of sub-horizontal S_2 foliation planes accompanied with recumbent isoclinal folds and NW–SE trending L_2 lineations. The main sense during D_2 was top-to-the-NW with local reversals to the SE. The third folding generations F_3 is recorded as axial plane S_3-surfaces and is characterized by open concentric folding that overprinting both F_1 and F_2 folds and has a flexural-slip mechanism. F_3 fold hinges plunge to the west–northwest or east–southeast indicate north–northeast–south–southwest shortening during D_3. The fourth deformational event D_4 is characterized by NE plunging open concentric folding overprint the pre-existing fold generations and formed under flexural slip mechanism reflecting coaxial deformation and indicating change in the stress regime as a result of the change in shortening from NE–SW to NW–SE. This phase is probably accompanied with the final assembly of east and west Gondwana. The dextral NW–SE shear zone that bounded the southwestern portion of the metamorphic belt is probably related to reactivation of the Najd fault system during Oligo-Miocene in South Sinai.

Keywords Kid metamorphic complex · Image processing · Shear zone · Structure analysis · Najd fault system

✉ Mohamed O. Arnous
arnous_72@yahoo.com;
mohamed.arnous@science.suez.edu.eg

[1] Geology Department, Faculty of Science, Port Said University, Port Said, Egypt

[2] Faculty of Earth Sciences, King Abdulaziz University, Jeddah, Saudi Arabia

[3] Geology Department, Faculty of Science, Suez Canal University, Ismailia, Egypt

Introduction

The Kid metamorphic complex (KMC) is an elongated NW-trending metamorphic complex of volcano-sedimentary succession. It is located directly to the southeastern part of Sinai between latitudes 28°27′ and 28°10′ and longitudes 34°10′ and 34°27′, covering a surface area of about 550 Km^2 (Fig. 1a). It is characterized by a thick succession of island arc sequence and classified into various Precambrian tectonostratigraphic units of distinct nature, contacts and extent (Shimron 1980; Reymer and Yogev 1983; Furnes et al. 1985; El-Gaby et al. 1991; Abu El-Enen 2008; Eliwa et al. 2008; Fowler et al. 2010a, b; Shalaby and Shawky 2014). The KMC underwent polyphase progressive deformation and metamorphism ranging from greenschist to upper amphibolite facies conditions (Reymer et al.

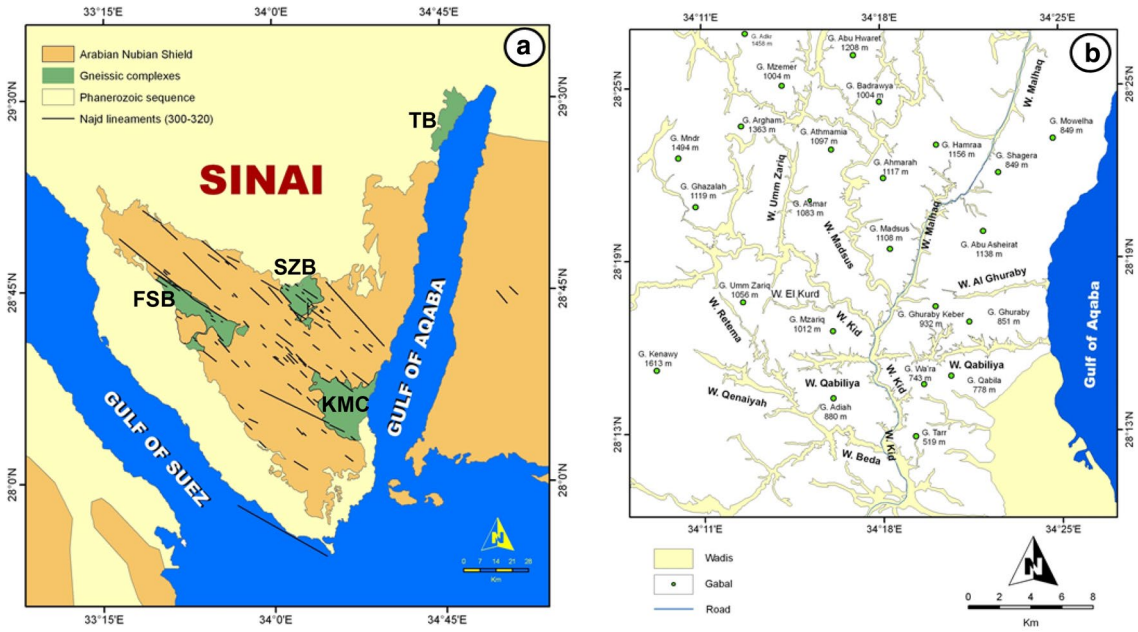

Fig. 1 Location and physiographic maps. **a** Location map showing South Sinai metamorphic belts: Taba belt (*TB*) and Kid metamorphic complex (*KMC*) are located on the Gulf of Aqaba, Feiran–Solaf belt (*FSB*) near the Gulf of Suez, whereas Sa'al Zaghraa belt (*SZB*) is located in the central part of South Sinai. Lineament pattern shown on the map is referred to Najd fault system in South Sinai; **b** Physiographic map of the study area shows the drainage system (Wadis/valleys; W) and the most peaks/mountain (G)

1984; Navon and Reymer 1984; Abu El-Enen and Makroum 2003; Brooijmans et al. 2003; Abu El-Enen et al. 2004). In addition, the regional metamorphism reached low P amphibolite facies conditions during D_2 (Halpern and Tristan 1981; Shimron 1984b; Reymer and Oertel 1985; Blasband et al. 1997; Fowler et al. 2010a, b). It is moderately rugged/mountainous and encompasses several major peaks (Fig. 1b).

The current study is field-based structural analysis aiming at reconstructing the tectonic history of KMC using remote sensing techniques. Resolving the extension of NFS in south Sinai is also considered.

Remote sensing data and enhancement methods

Landsat Enhancement Thematic Mapper Plus (ETM^+) data, ASTER GDEM, and IKONOS images acquired from Google Earth. These data were digitally processed using ERDAS imagine 9.2 and ArcGIS 9.3.1 software to discriminate and map the lithological units and the structural features. The Landsat ETM^+ 7 scene acquired in the late summer season (September 2000) covering the investigated area have been radiometrically balanced and processed. Many techniques of image enhancement are applied to achieve the best methods used to identify the different rock units. These methods comprise, band rationing, convolution filters, principal component analysis (PCA), and contrast stretching. On the other hand, the directional filtering of (ETM^+ 7) and hill shade technique and classified elevation of ASTER GDEM and IKONOS images are used to extract the major lineaments of the study area. Interpretation of the enhanced space-borne data depends typically on the spectral signatures of the earth resources on the land cover and its physical and chemical composition. The space-born data of the present work include a Landsat ETM^+ 7 dated 2000 for path 174/row 40 with the spatial resolution 15 m after resolution merges of multispectral and panchromatic bands. The image is cloud free and it was rectified into a UTM projection.

Band ratios are utilized for the rock unit identification in a space-borne data where the various minerals reflect more brightly at various wavelength and exact ratios can identify the relative dissimilarity in reflectance values (Sultan et al. 1987a, b; Kusky and Ramadan 2002; Inzana et al. 2003; Gad and Kusky 2006; Gad 2007; Sultan 2011; Arnous and Sultan 2014; Arnous 2016). The specific band ratios such as (3/4, 5/4, 5/7, and 5/1) are affected by the physical and chemical composition of the constituents rock minerals (Sultan et al. 1987a, b). The IKONOS images are used in the current study as base maps for detailed field investigation. They also used to verify the geological contacts of enhanced ETM^+ 7 and to extract structural lineaments.

Image processing analysis

The correlation coefficient and the scatterograms of the study area show that the lowest correlation is between bands 1 and 7 followed by bands 1 and 5. On the other hand, the correlation between the two infrared bands 5 and 7 is very strong; therefore, band 5 is excluded. Obviously, the correlation among the three, visible bands 1, 2, 3 are very high as a true color composite image in RGB. Therefore, bands 2 and 3 are also excluded. Correlation between band 1 and band 4 and also between band 7 and band 4 are weak. Consequently, the optimum triple band combination that is less correlated and contains abundant information with lowest or no redundancies are bands 7, 4, 1 that are assigned to RGB pseudocolor band combination, respectively. Different rock units are expressed by different colors; for instance, granitoids appear as yellowish brown (2 in Fig. 2), whereas metavolcanics and metasediments appear as reddish brown (1 in Fig. 2), while the pyroclastics appear as green color (Fig. 2).

Principal component analysis

The eigenvectors results of the six principal components (PCs) of the enhanced ETM$^+$ image (Fig. 3) clarify that the (PC4) is highly loaded with band 7 (66%) and also (PC5) is highly loaded with band 4 (66%). The visual view

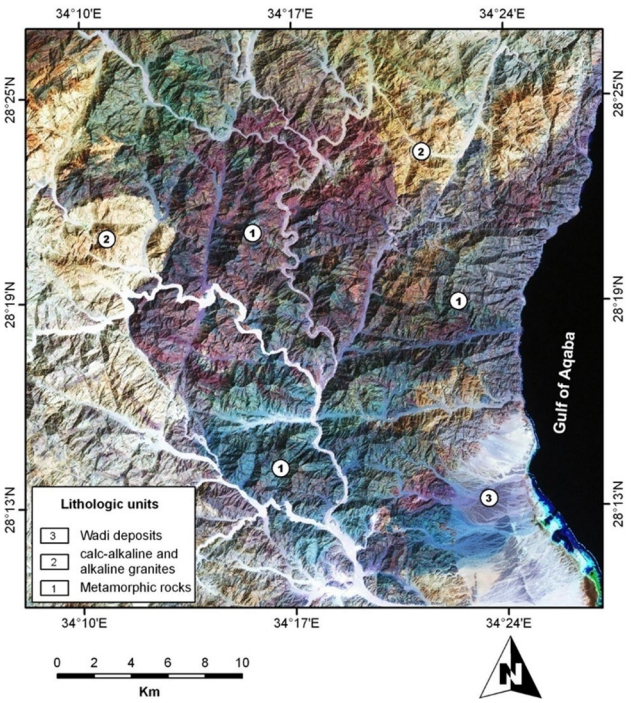

Fig. 2 Landsat ETM$^+$ 7 (FCC) image (*bands 7, 4, 1* in R, G, B) of the Kid metamorphic complex

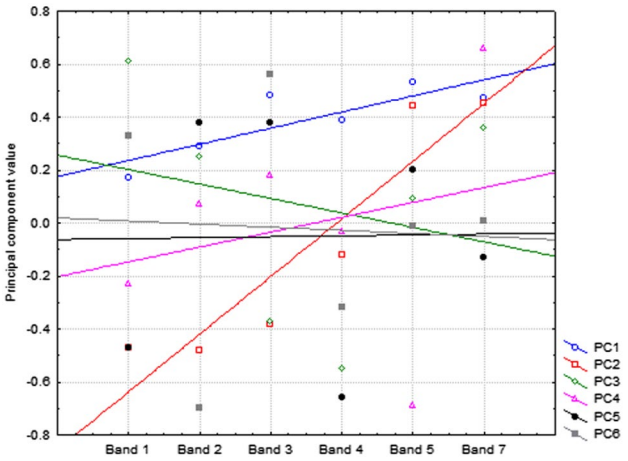

Fig. 3 Statistical relationship between eigenvectors of six principal components of the enhanced Landsat ETM$^+$ 7 image

of the fifth principal component is excluded, because it is failed to discriminate the different types of the metamorphic rocks (Fig. 4). The third principal component is highly loaded with band 4 (55%) and the (PC2) is highly loaded with band 1 (47%). On the other hand, the visual comparison of each principal component image confirms the results of the eigenvectors, in which PC4, PC3, and PC2 in RGB respectively are the best principal components for lithologic mapping.

The composite image (Fig. 5) of PC4, PC3, and PC2 in RGB discriminates the mapped rock units in KMC area, where the metavolcanics have reddish brown color, the metasediments appear in bluish green to pale light tan color, the Dokhan volcanics appear in dark reddish brown color, the metadiorite appears in yellowish green color, metagabbro-diorite complex appears in pale reddish green color, granitic orthogneiss appear in sky blue color, the quartz diorite and gabbro appear in purple color, the calc-alkaline appears in sky blue color, and the alkali granite appears in purple to white blue color (Fig. 5).

Band ratio

Band ratio combination 4/2, 5/4, 7/5 in RGB and band ratio combination 5/7, 4/5, 3/1 in RGB are respectively utilized to display different lithological units and depict sharp contrast among them. The band ratio 4/2, 5/4, and 7/5 in RGB (Fig. 6) clearly display and increase the number of the exposed rock units. In Fig. 6, the metasediments appear as pale sky blue to pale green color, the metavolcanics appear in dark blue, the Dokhan volcanic appears in dark red, the metadiorite appears in blue, metagabbro-diorite complex appears in pinkish blue, granitic orthogneiss appear in greenish yellow, quartz diorite and gabbro appear in pale blue, the calc-alkaline appears in yellow to greenish yellow,

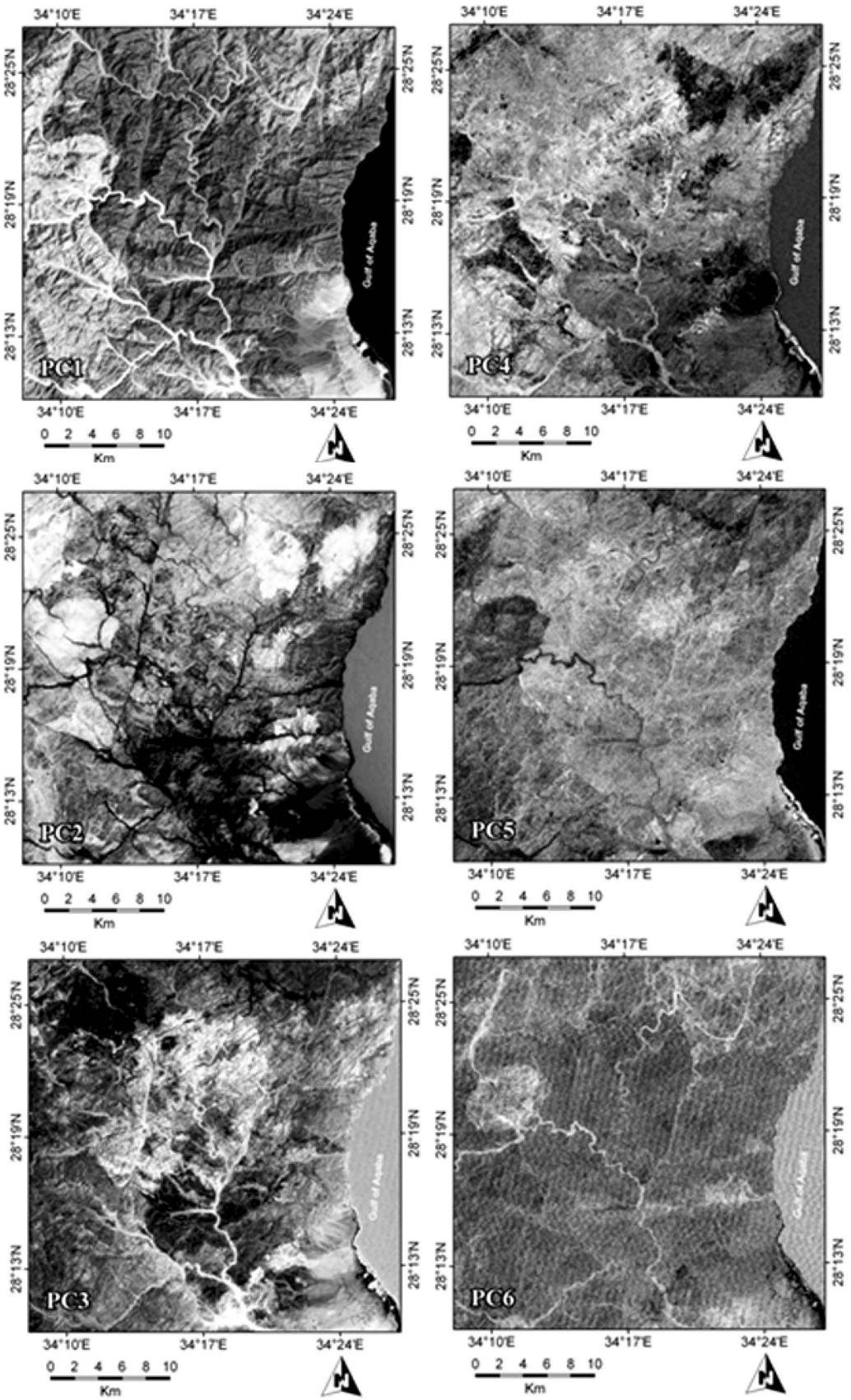

Fig. 4 Landsat ETM$^+$ 7 of the PCA enhanced images of the Kid metamorphic complex

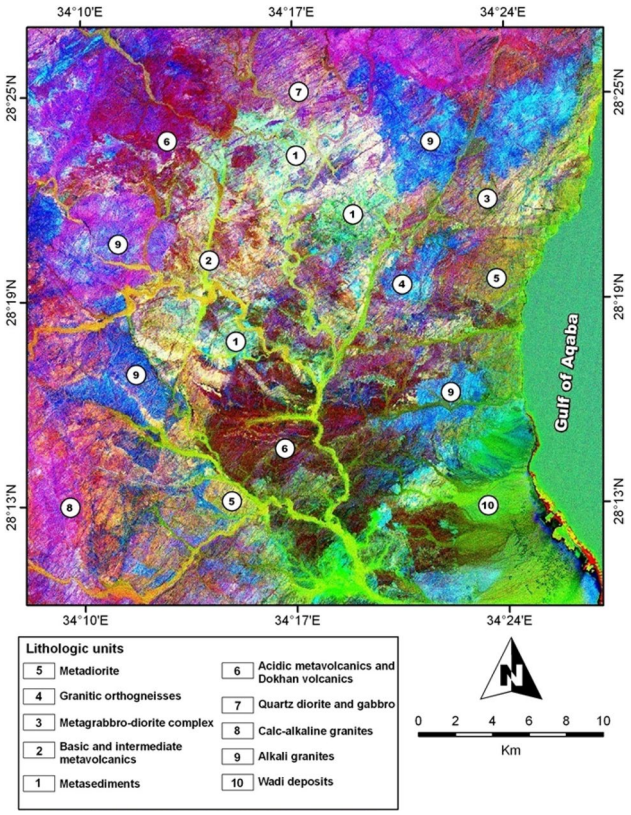

Fig. 5 Landsat ETM$^+$ 7 principal component image (PC4, PC3, and PC2 in RGB) of the mapped area

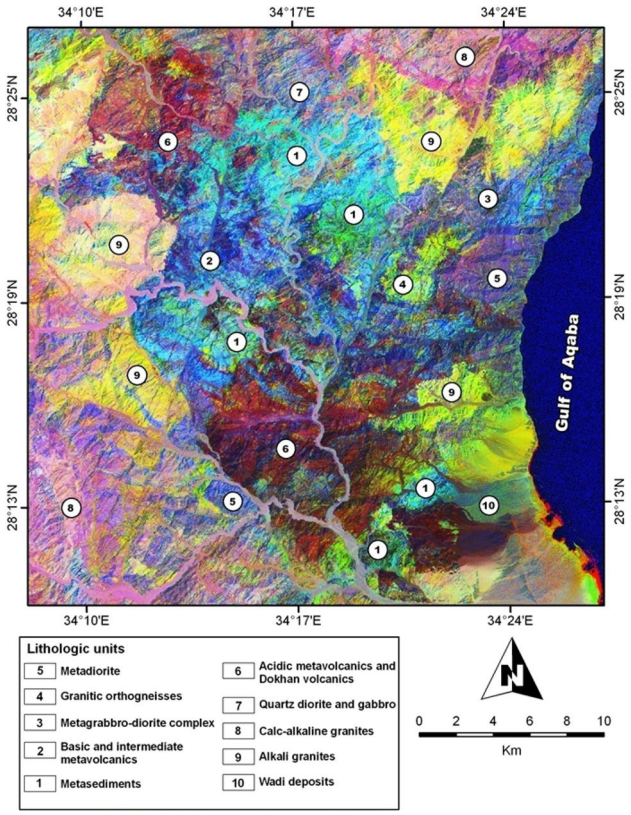

Fig. 6 Enhanced band ratio Landsat ETM$^+$ 7 image (4/2–5/4–7/5 in RGB) of the mapped area

and the alkali granite appears in pink color, while the band ratios 5/7, 4/5, and 3/1 in RGB (Fig. 7) are successfully discriminate the different rock units shown in Fig. 6. Whereas, metavolcanics have green to dark green color, the metasediments appear in dark reddish blue, the Dokhan volcanics appear in yellow, the metadiorite appears in pale green to dark green, metagabbro-diorite complex appears in pale green to pale blue, granitic orthogneiss appear in red, quartz diorite and gabbro appear in pale green to pale blue, the calc-alkaline appears in purple to red, and the alkali granite appears in blue color.

The discriminated rock units were verified in the field. The enhanced images carried out during the present study are visibly discriminate between metavolcanics and metasediments occupied to the northern part of the KMC area. The enhanced ASTER images of Gad and Kusky (2006) and Gad (2007) interpreted some of the granitic bodies as meta-pyroclastic. The ETM$^+$ 7 satellite image used in this study discriminates between them easily.

Lineament extractions

Lineaments are extracted and analyzed based on the enhanced space-borne data, GIS, and integrated with the geometric approaches of structural geology (Fig. 8a). The Landsat 7 ETM$^+$ and the IKONOS satellite images are utilized in the current work to conduct detailed analysis of structural lineaments such as dikes and faults. Different convolution kernels are applied to the satellite images to extract the major and minor structural lineaments such as low-pass frequency, directional filters, and compass gradient convolutions (Süzen and Toprak 1998; Koike et al. 1995; Mah et al. 1995; Novak and Soulakellis 2000; Arnous and Green 2011; Arnous 2011). For lineaments extraction, the ETM$^+$ 7 image is first smoothed with an average low-pass filter to reduce the noise. Following the smoothing process, directional filtering method is selected for lineament extraction, because the directional nature of Sobel kernels generates an effective and faster way to evaluate the lineaments in four principal directions (Süzen and Toprak 1998). The Sobel kernels in four principal trend directions in the processed images of the study area are given in Table 1.

The enhanced satellite data was calibrated by field data and then combined to prepare the digital geological map of KMC. The structural lineaments of KMC were extracted and digitized throughout various enhanced space-borne data (Fig. 8a). The lengths of the extracted structural

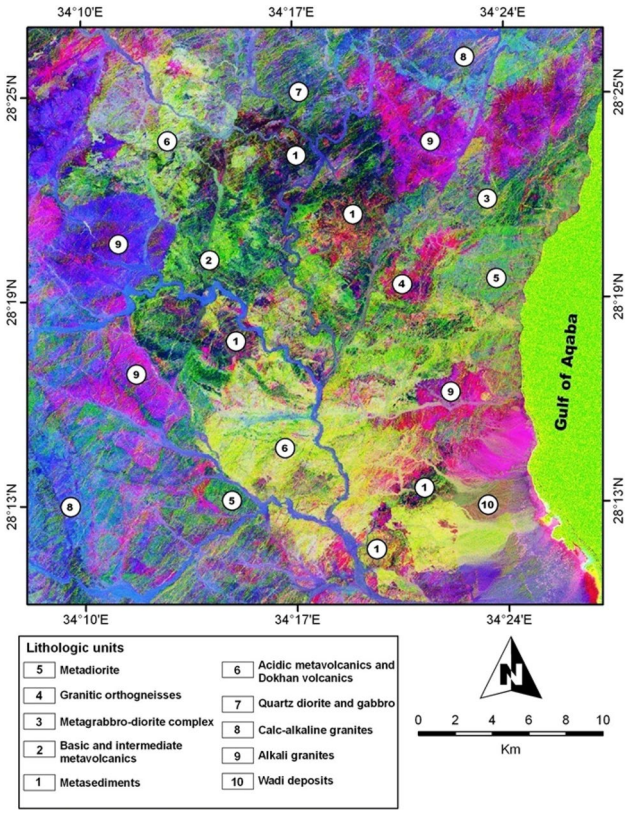

Fig. 7 Enhanced band ratio Landsat ETM$^+$ 7 image (5/7–4/5–3/1 in RGB) of the mapped area

lineaments are measured and interpreted. On the other hand, the lithologic units were digitally processed within the ARC GIS software. The linear features such as the geologic contacts between adjacent lithologic units, folding axial traces, regional faults, fractures, and bedding planes can be recognized on the enhanced filtering images.

The extracted lineament are plotted on the rose diagram for displaying the dominant fracture sets (Fig. 8b). They are trending towards N30°–40°E, N40°–50°E, N50°–60°E and N40°–50°W. The NE-trends are delineate the dike swarms that crosscut the entire KMC and the surrounding granitoids, while NNE and NW trends are mainly fault lineaments and major fold axial traces.

Geological setting

The Kid metamorphic complex is composed essentially of nine lithological units based on the enhanced ETM images, their spatial distribution, and the structural patterns. The geological map was created previously by many authors such as Shimron (1980, 1984a), El-Metwally et al. (1999) and El-Bialy (2010). The accurate of the constructed geological map of the present study is well matched to the geological map of El-Bialy (2010), in which the metasediments, metavolcanics, metadiorite, and granitoids are near to be with the same distribution. The stratigraphic succession is arranged based on the field relationships into:

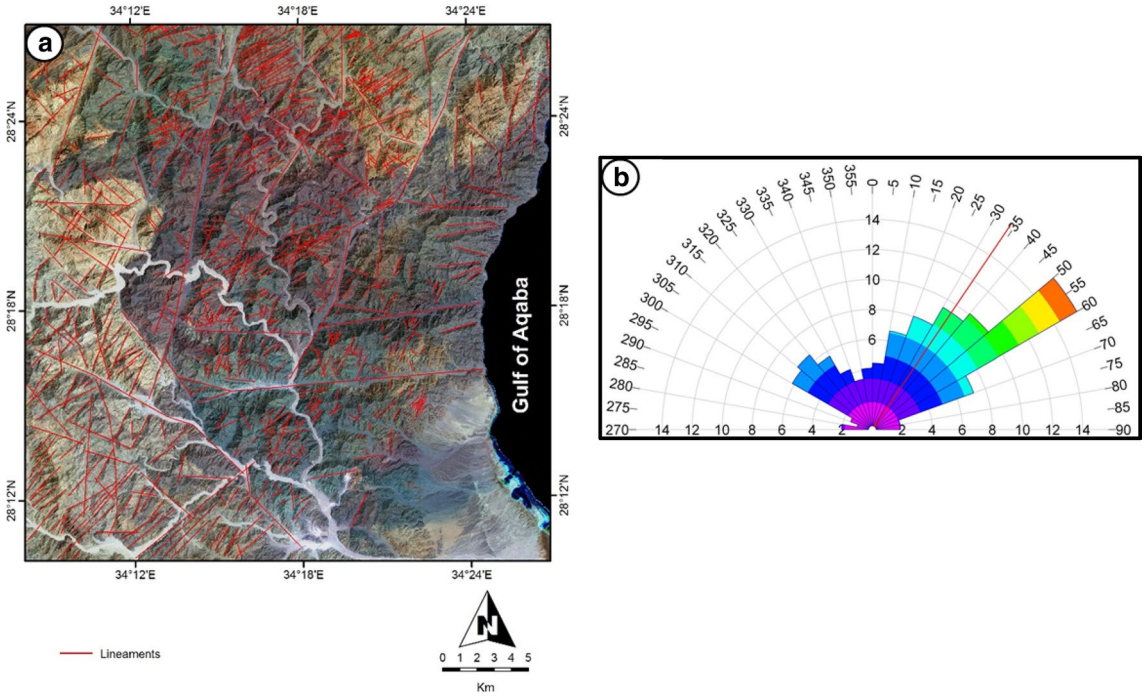

Fig. 8 **a** Structural lineaments map of the entire Kid area interpreted from enhanced ETM$^+$ 7 and IKONOS satellite images; **b** *rose diagram* showing trends of fracture lineaments extracted from satellite images

Table 1 Sobel kernels in four principal directions

N–S			NE–SW			E–W			NW–SE		
−1	0	1	−2	−1	−0	−1	−2	−1	0	1	2
−2	0	2	−1	0	1	0	0	0	−1	0	1
−1	0	1	0	1	2	1	2	1	−2	−1	0

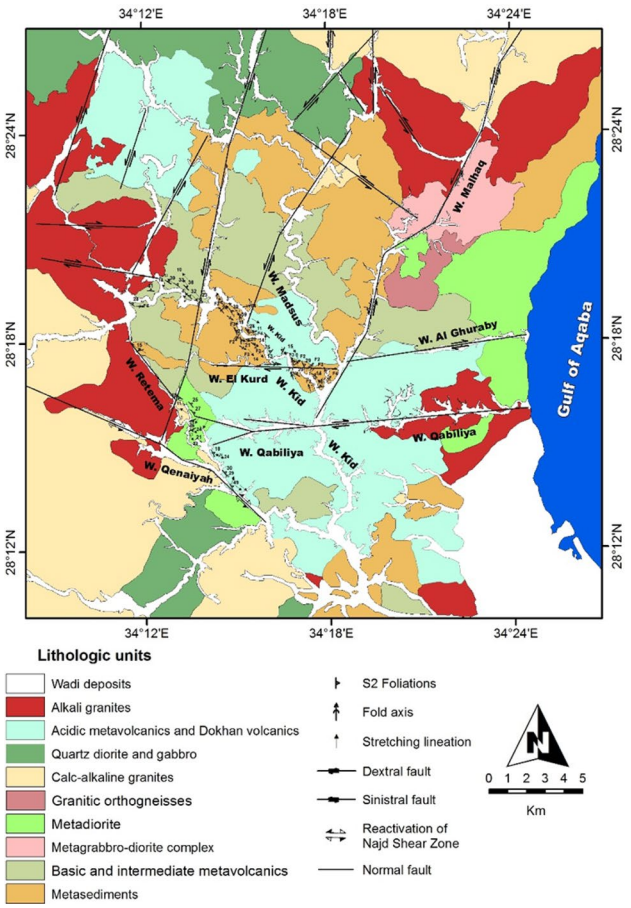

Fig. 9 Geologic map of the Kid metamorphic complex showing the major faults (rock units nomenclatures are modified after El-Bialy 2009)

metasediments, basic and intermediate metavolcanics, acidic metavolcanics, metagabbro-diorite complex, metadiorite, orthogneisses, calc-alkaline granitoids, dokhan volcanics, alkaline granites, and associated dike swarms (Fig. 9).

Metasediments represent about 50% of the exposed units. These were designated by El-Metwally et al. (1999) as meta-calcpelites and meta-psammopelites. Meta-calcpelites comprise banded para-amphibolites, and hornblende and chlorite schist, while meta-psammopelites contain garnetiferous biotite schist and phyllite. The above-mentioned metasediments comprise Umm Zariq Formation (Furnes et al. 1985; Abu El-Enen et al. 2003), Heib Formation, and most of Malhaq Formation (Shimron 1980). On the other hand, the metasediments exposed around the downstream of W. Kid (Fig. 9) are prevailing a metasedimentary sequence of low-grade schists, metaconglomerates, metamudstones, and metasandstones. This sedimentary sequence was referred to as Tarr Formation by Shimron (1980, 1983).

The intermediate and basic metavolcanic rocks are of greenschist to amphibolites facies. They were originally lava flows, ranging from basalts to andesites (Furnes et al. 1985) (Fig. 10). In hand specimen, they are either aphyric or fairly porphyritic with scattered plagioclase phenocrysts (andesites). The lower lava flow sheets in this unit are interbedded with and overlying the above-mentioned thick metasedimentary succession (Fig. 10a). The grade of metamorphism decreases upward in these metavolcanics, and the rocks of the upper horizons are relatively fresh or weakly metamorphosed to the lower greenschist facies (Hassanen 1992).

The acidic metavolcanics are of greenschist facies silicic porphyritic volcanics (typically rhyolites). They include lavas, ignimbrites, and lapilli tuffs. The metagabbro-diorite complex (Fig. 9) occurs as a single large intrusive body in the northern part of the Kid-Malhaq region. It was namely as "Shahira gabbro and diorite complex" by Furnes et al. (1985) who described it as a layered gabbroic and dioritic layered intrusive massif of at least 2000 m thick and was dated at 570 ± 4 Ma by Moghazi et al. (1998).

Metadiorite located in the SW and NE borders of the KMC. It consists of foliated and lineated diorite and granodiorite with occasional mafic–rich xenoliths and locally mylonitized (Fig. 11). These gneisses were referred to as Qenaia Formation by Bentor and Eyal (1987) and are considered of plutonic origin (Brooijmans et al. 2003 and; Be'eri-Shlevin et al. 2009) and intruded during the peak of high grade metamorphism (Reymer and Yogev 1983; Fowler et al. 2010). The metadiorite exposed along W. Retema was sinistraly separated into two blocks by the Qenaiyah Fault (Fig. 9).

Granite orthogneisses are highly metamorphosed orthogneisses and locally exposed in the eastern side of W. Malhaq nearby the metadiorite (Fig. 9). The calc-alkaline granites intruded and bounded the volcano-sedimentary successions (Fig. 9). Monzogranite and syno-granite were emplaced within the successions in W. Qabiliya and

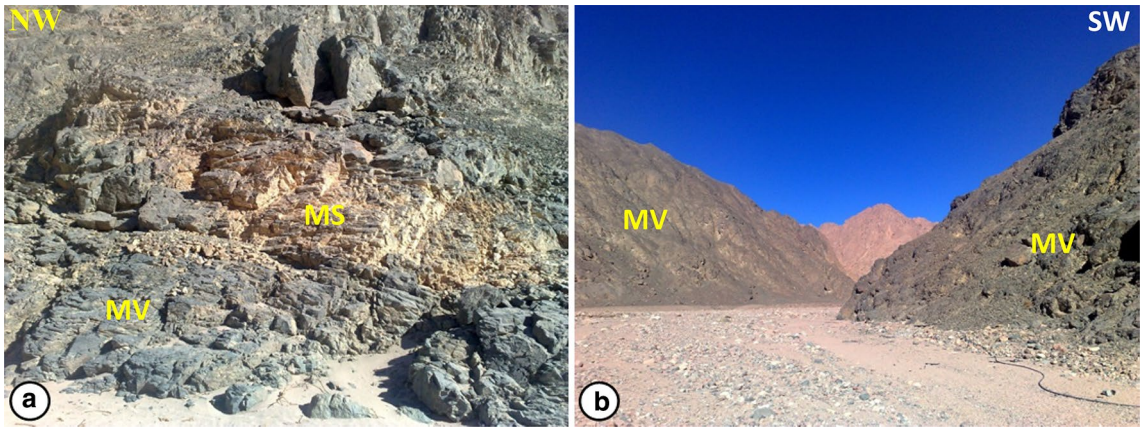

Fig. 10 Field photographs of the common metamorphic rocks and the associated granitic bodies. **a** Metasediments (*MS*) intercalated with metavolcanics (*MV*); **b** metavolcanics (*MV*), intruded by G. Ghazalah calc-alkaline granitoids (G)

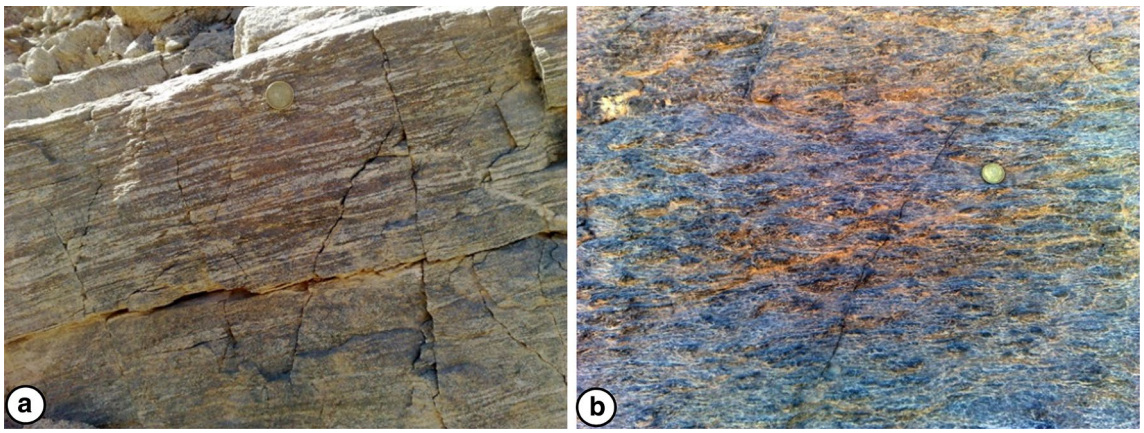

Fig. 11 Field photographs of metadiorites: **a** well-developed gneissic banding in metadiorite, W. Retema; **b** stretched mineral lineations in metadiorite, W. Retema. *Scale* coin = 2.0 cm diameter

dislocated by dextral fault associated with the Gulf of Aqaba-Dead sea transform fault.

The Dokhan volcanics in the KMC area are located with the acidic metavolcanics (Fig. 9). They consist of unmetamorphosed, vary colored, succession, and are porphyritic lava flows and generally felsic (El-Metwally et al. 1999). They are interlayered with compositionally equivalent pyroclastic beds (dominantly ignimbrites). Lava flows predominate in this volcanic suite, comprising chiefly of rhyolites with subordinate dacites and trachydacites. They intruded at 609 ± 12 Ma (Bielski 1982) and display geochemical characteristics of both orogenic arc-type and an orogenic within plate environments, suggesting eruption in a transitional "post-collisional tectonic setting (El-Bialy 2010).

Alkaline granites are the youngest plutonic intrusion in the mapped area (Figs. 9, 12a). It is exposed in several locations intruding and along the boundary of the metamorphic complex. In general, the KMC is dissected by vertical felsic and mafic dike swarms of Precambrian age. They strike N30°E–N60°E (Fig. 12b). Both types of dikes intruded at 590–580 Ma (Halpern 1980; Stern and Manton 1987).

Metamorphism

Metamorphic grades of the Wadi Kid area range lower greenschist to amphibolite facies with a general increasing trend towards the central and northern parts of the mapped area. Lower–greenschist–facies rocks dominate the southern part. While in the central part of the mapped area, the sillimanite, garnet, and andalusite porphyroblasts were detected and the metamorphic grade reaches upper

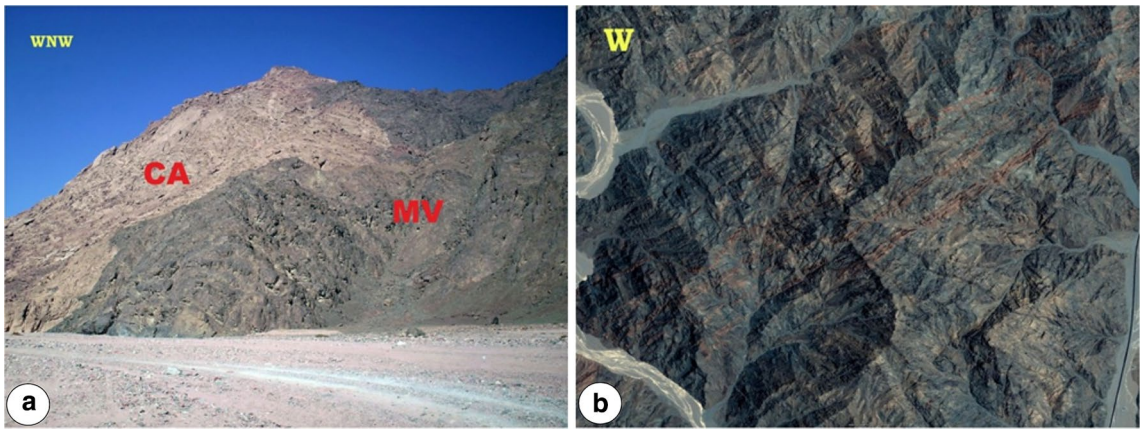

Fig. 12 Granitic intrusion and dike swarms: **a** metavolcanics (*MV*) intruded by calc-alkaline granitoids (*CA*) at the upstream of W. Kid; **b** IKONOS image of metasediments and metavolcanics intruded by NE-trending dike swarms

amphibolite facies (Blasband et al. 2000). The metavolcanic rocks are exposed at the northern part of the area and have garnet and hornblende porphyroblasts. The central part of the mapped area attained a temperature of 700 °C and a pressure of 3–4 kbar (Blasband et al. 2000). The metamorphic grade increases in the biotite-schists from lower to higher greenschist facies. Migmatites are exposed locally in the north-western part of the mapped area at the upstream of W. Kid and W. Retema nearby the alkali granite (Fig. 9).

Structural setting of the KMC

The area under study has a complex tectonic history and different structural elements. These elements are used to construct the evolution history of the area. Foliations, lineations, faults, folds, and shear zones are the main recognized structural features (Fig. 13).

Foliations

The foliation planes preserved in the metasedimentary units are penetrative and defined by the preferred orientation of micas and/or amphiboles. It is developed with varying intensity from slaty cleavage to schistosity (Fig. 14). Metavolcanics and metatuffs exhibit less developed foliation. These foliations describe the S_2 where S_1 foliations are weak (Fig. 14a), and found only in the hinge zones of the major F_1 folds. The S_2 foliations are flat-lying to gently dipping <30° (Fig. 14b). The S_2 foliations are extended through the metadiorite, indicating that the metadiorite was intruded before the development of S_2 (Blasband et al. 1997). It is produced by pure flattening strain (Reymer and Oertel 1985; Fowler et al. 2010a, b).

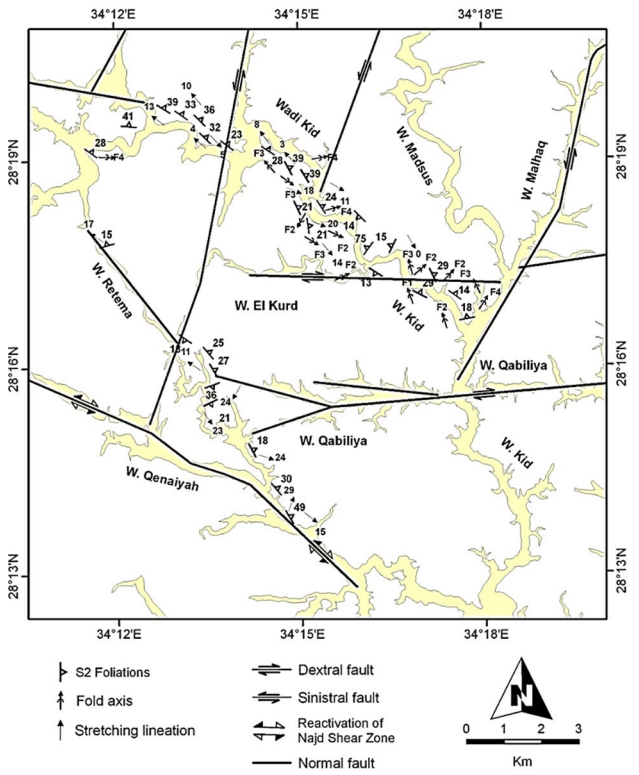

Fig. 13 Structural map of the Kid metamorphic complex showing the main structural elements

Geometrically, the poles of S_2-surfaces; the main foliations in the study area are measured in the KMC and projected and contoured on an equal-area stereoplot using a constant contour interval (Fig. 15). Poles to S_2-surfaces are represented by one maximum and reflecting the subhorizontality of S_2 foliations (Fig. 15).

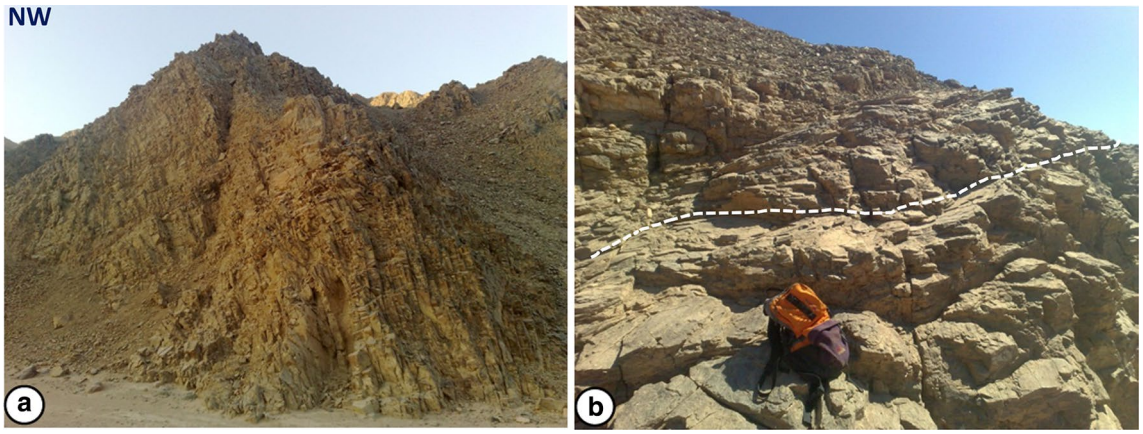

Fig. 14 Field photographs of S_1 and S_2 foliations: **a** NE-striking and steeply SE dipping S_1 foliations in slate, W. Beda (width of view is 40 m); **b** sub-horizontal S_2 foliations (*dashed line*) in schist; looking NW

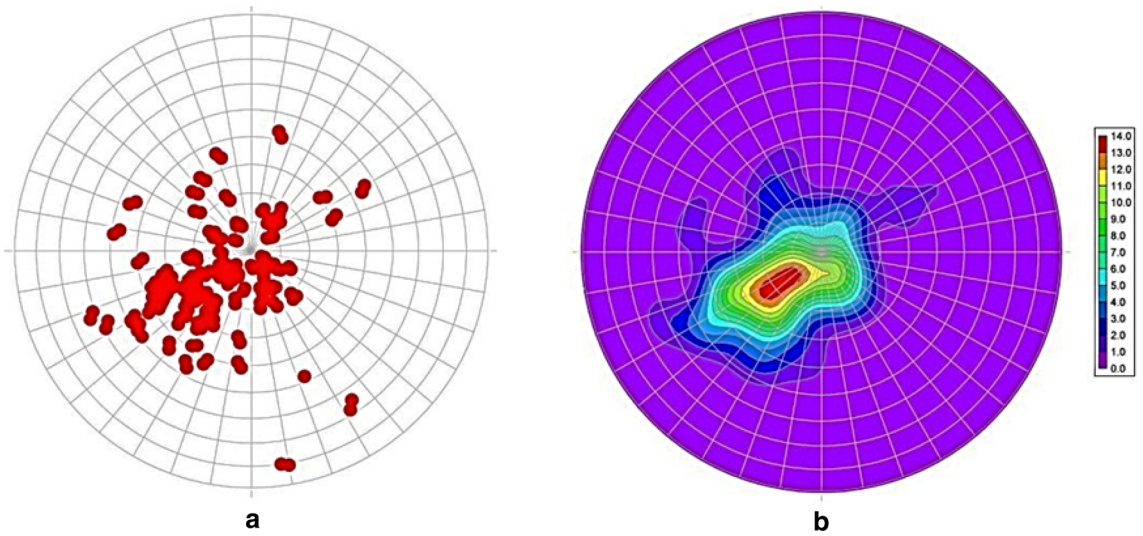

Fig. 15 Lower hemisphere equal-area projection. **a** Pole diagram of the measured S_2 foliation planes in the KMC; **b** contour equivalent shows gently to sub-horizontal NE–SW striking foliations planes

Shear zones and shear sense indicators

Ductile and brittle shear zone with several shear sense indicators are recorded in the study area. They are low angle shear zones of the second deformation and display a dominant dextral NW Shear sense indicators, and they are representing the late stage of shearing event overprinting the early coaxial development of S_2 foliations. The sense of shear was determined through porphyroclasts (as in Mukherjee 2010a, b, 2013a, b, 2014a, 2015; Mukherjee and Koyi 2010a), rotated boudin lines (see Mukherjee 2014b), and asymmetric folds (as in Mukherjee et al. 2015). These asymmetric structures display the movement direction either top-to-the-NW (Fig. 16a) or top-to-the-SE (Fig. 16b). Reverse shear sense with shear zone seems to be not uncommon (as in Mukherjee and Koyi 2010b). The thrust-related ductile shear zones with top-to-the-NW are characterized by s-shaped structures (Fig. 16a), σ-type (Fig. 16b), and local synthetic minor faults associated with asymmetric boudins (Fig. 16c). The thrust-related ductile shear zones with top-to-the-SE are characterized by σ-type (Fig. 16d). Symmetric structures not containing any shear sense exist (as in Mukherjee 2016), but those are not described here. Ductile shear bands (Fig. 17a) in metasediments and en-echelon quartz vein array (Fig. 17b) indicating dextral brittle shear movement direction in the metasediments with top-to-the-SE.

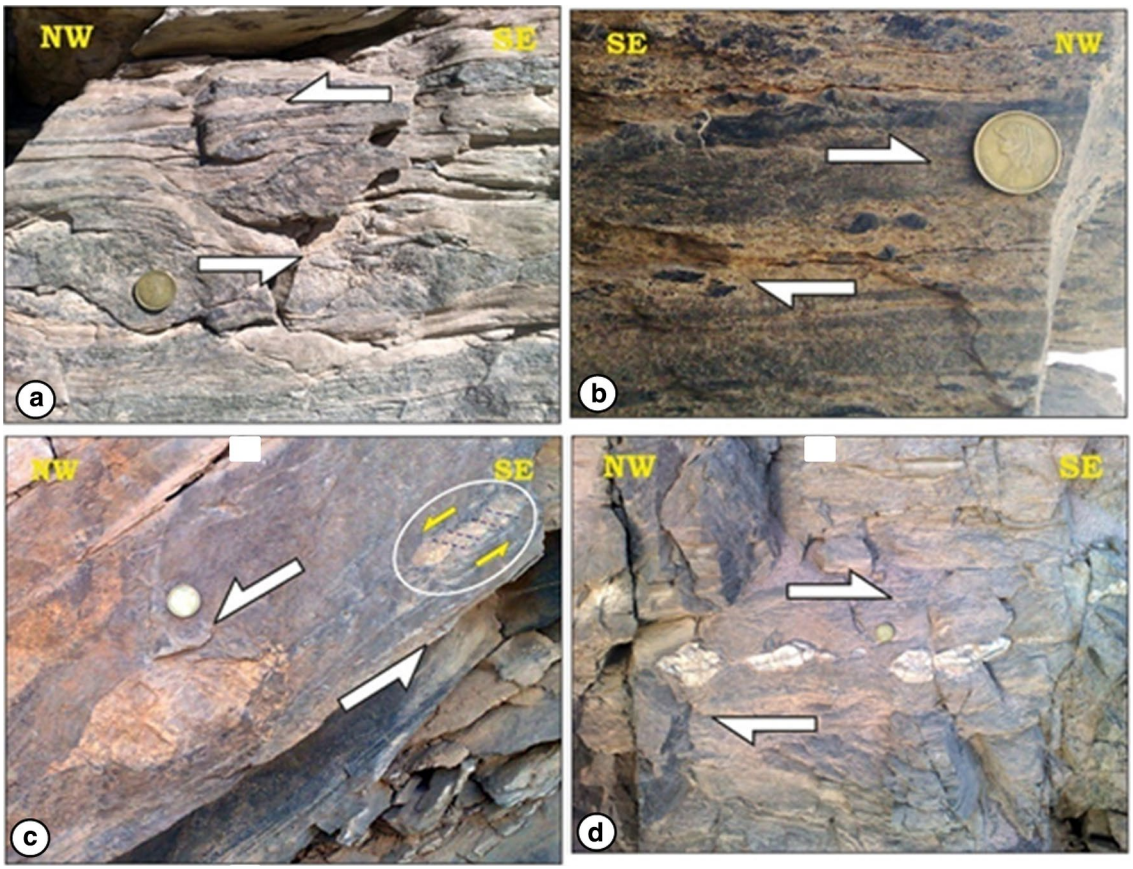

Fig. 16 Field photographs of thrust-related ductile shear zones with top-to-the-NW. **a** σ-Type porphyroclast showing sinisterly sense of shear; **b** σ-type porphyroclast showing dextral sense of shear in metasediments; **c** synthetic microfaults "*white circle*" and the associated *asymmetric boudins* indicating sinistral ductile shear zone in metasediments; **d** deformed quartz vein showing σ-type *boudin lines* with dextral ductile shearing in metasediments "top-to-the-SE". *Scale* coin = 2.0 cm diameter

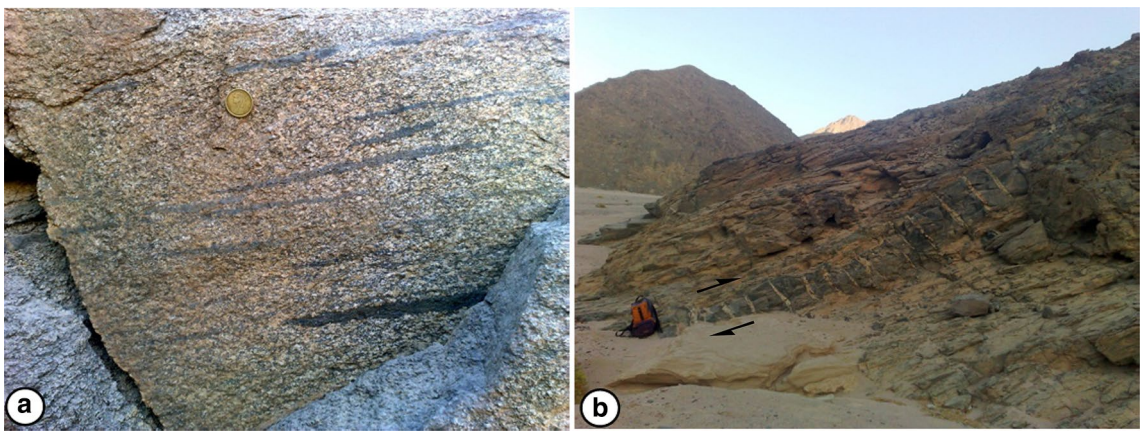

Fig. 17 Field photographs of ductile and brittle shear. **a** Sub-parallel amphibolite shear bands in metasediments; **b** en-echelon quartz *vein array* indicating dextral brittle shear in metasediments with top-to-the-SE. Looking NE

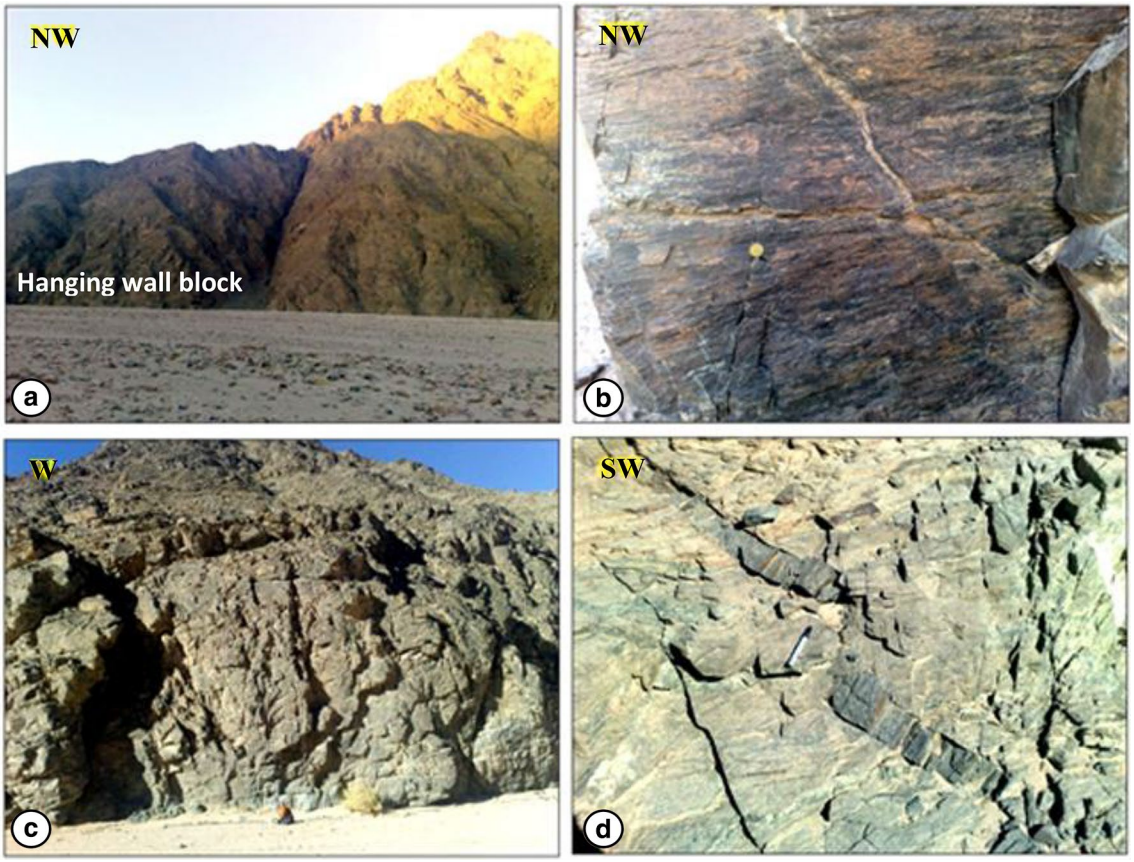

Fig. 18 Field photographs of different types of faults cross cut the Kid metamorphic complex. **a** NW-dipping normal fault in metasedimnets, width of view is about 100 m; **b** slickensides of left lateral NW strike-slip fault in metasediments; **c** side view wall of W. Qabiliya showing slicken sides of right lateral strike-slip fault in metasediments; **d** right lateral NE–SW strike-slip fault of a NW–SE dike in the metasediments

Faults

The rock units of the mapped area are dislocated by varieties of faults (Fig. 9). Several high angle normal faults striking NNE to NE crosscutting the S_2 foliations (Fig. 18a). A group of sinistral and dextral strike-slip faults cross cut the investigated area, both at macroscopic (Fig. 18b, c) and mesoscopic scale (Fig. 18d). The strikes of the sinistral faults are sub-parallel to the Gulf of Aqaba transform fault as in W. Mahlaq, while there conjugate dextral faults strikies normal to the Gulf of Aqaba as in W. Qabiliya (Figs. 9, 13).

Stretching lineations

The stretching lineations are well developed on S_2 foliation planes. The lineations is sub-horizontal (<30°), plunging either NW or SE due to the effect of later folding (Fig. 19). The two trends reflect one strain regime. The stretching lineation throughout the mapped area are defined by the long axes of the stretched minerals or pebbles (Passchier and Trouw 1996). Geometrically, the attitude of stretched pebbles and mineral lineations are plotted and contoured on a stereogram (Fig. 20). The stereogram shows two maxima, the first one plunging 9° on a bearing N44°W, while the second maximum plunging 4° on a bearing S47°E. Shear sense indicators reveal that the NW–SE stretching lineations define the orientation of thrust-related ductile shear zones indicating a compressional tectonics (Fig. 19a). A contour diagram (Fig. 20a) shows the NW–SE trends of the plotted stretched lineations. Small folds are separated into four generations (F_1–F_4) based on the field interference pattern. The first one is very scarce and it is not plotted. The second generation of folding is a non-cylindrical fold and shows random distribution (Fig. 20b). The third generation of folding shows two groups, the first one has gentle plunge towards WNW, and the second one plunge gently towards the ESE (Fig. 20c). They are scattered by the effect of one more folding phase which is F_4. The plotting of F_4 folds shows one cluster; they plunges gently towards the NNE (Fig. 20d).

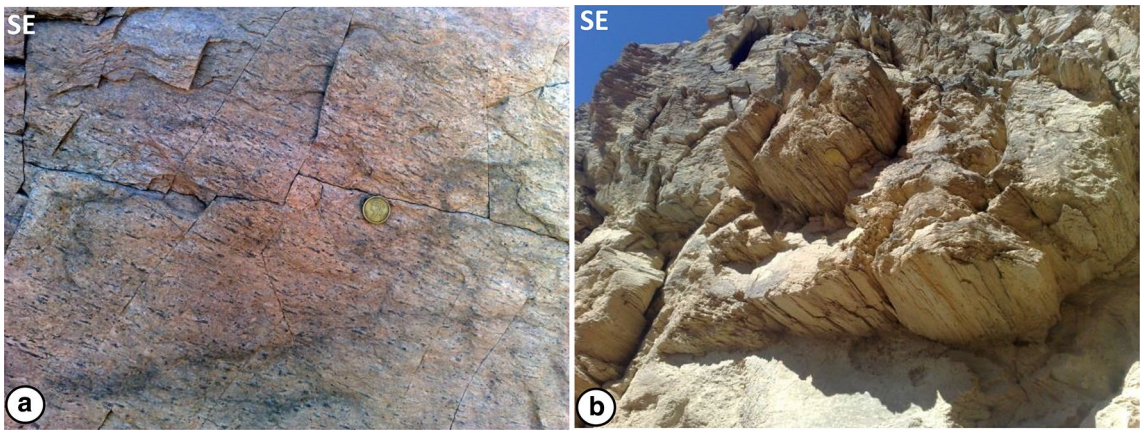

Fig. 19 Field photographs of lineations. **a** Stretched mineral lineations in metasediments. *Scale* coin = 2.0 cm diameter; **b** rod structure in metasediments developed steeply on the S_2 foliations. Width of view about 75 cm

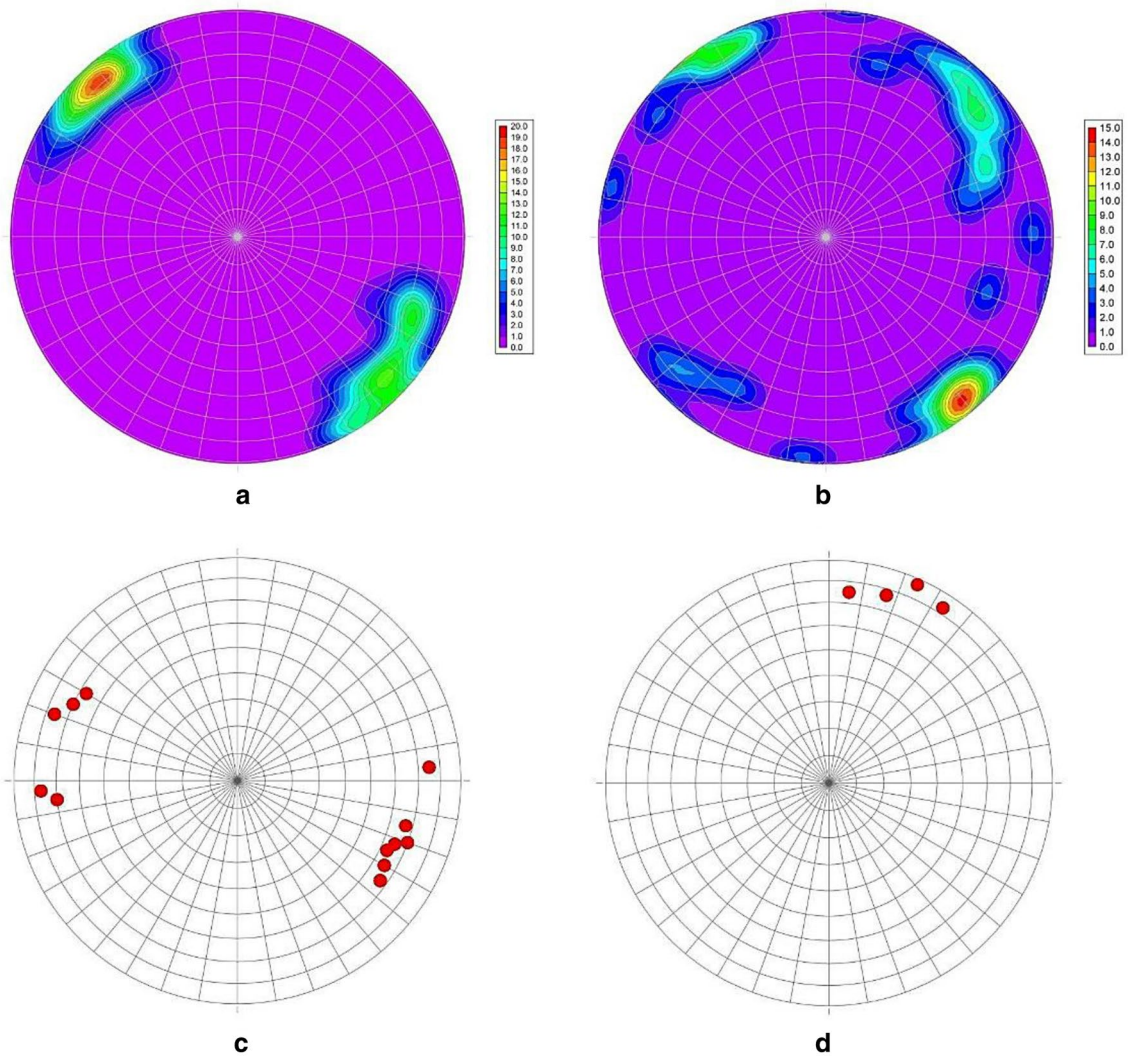

Fig. 20 Stereoplots of the main linear elements in the study area. **a** Contour diagram of the stretching lineations; **b** contour diagram of F_2 fold hinges; **c** point diagram of F_3 fold hinges; **d** point diagram of F_4 fold hinges

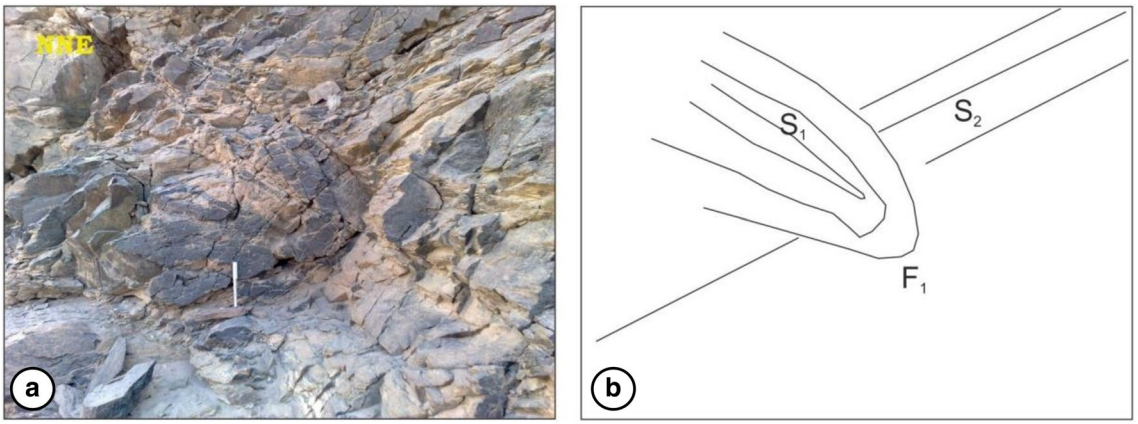

Fig. 21 Field photograph of F_1 fold **a** F_1 isoclinal fold in metasediments. **b** Traced sketch of (**a**) showing NE–SW S_1 axial plane foliation of the NE-trend F_1 fold and S_2 foliations

Fold generations

Four phases of folding are recognized within the entire mapped area. The oldest phase of folding is F_1. It is characterized by upright tight to isoclinal folds with sub-vertical S_1 foliations (Fig. 21). The second phase of folding F_2 is common and is represented by non-cylindrical semi-recumbent tight to isoclinal folds (Fig. 22). The hinges of the folds are gently plunging and have variable trends (Fig. 22). The third phase of deformation is described as open concentric folds (Fig. 23); it has a flexural slip nature and overprinting both F_1 and F_2 folds. The fourth phase of folding has also described as open concentric folds (Fig. 23c) and overprinting the early formed folds of F_1, F_2, and F_3; it has also a flexural slip mechanism. The area under investigation shows few interference patterns (Fig. 23d) where F_2 recumbent isoclinal folds refolded by F_3 open concentric folds.

Tectonic evolution of KMC

Based on field relations and geometrical analysis of the recorded structural elements in the KMC area, it may conclude that the tectonic history is passed through four successive deformational phases (D_1–D_4; Fig. 24). D_1 is broadly considered as an upright tight to isoclinal macroscopic folding with F_1 mesoscopic folds and sub-vertical S_1 axial plane foliation. This phase is thought to have been related to arc-accretion. The second deformational event D_2 is characterized by the regionally dominant shallow dipping S_2 foliation planes accompanied with

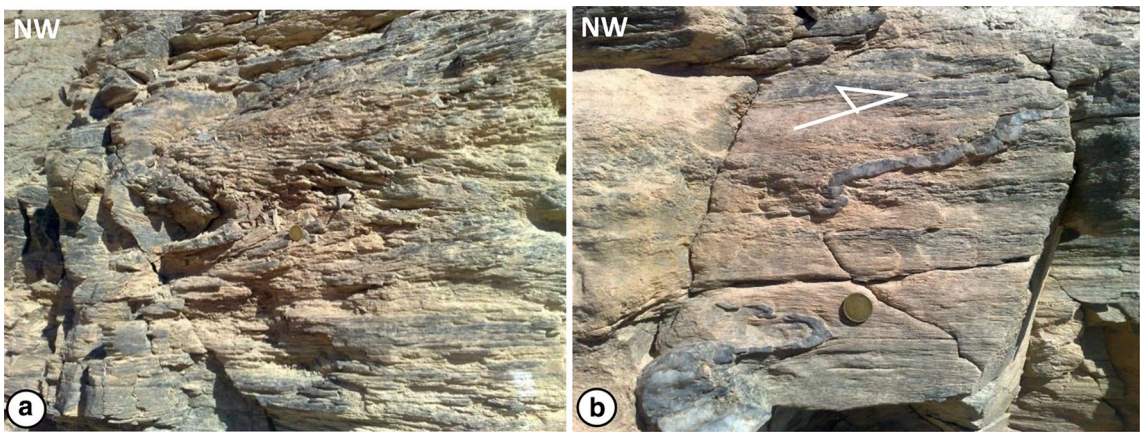

Fig. 22 Field photographs of F_2 folds in metasediments. **a** Recumbent isoclinals F_2 fold terminated by S_2-surfaces; **b** side view showing F_2 recumbent isoclinals fold and an asymmetrical s-shaped fold "top-to-the-NW". *Scale* coin = 2.0 cm diameter

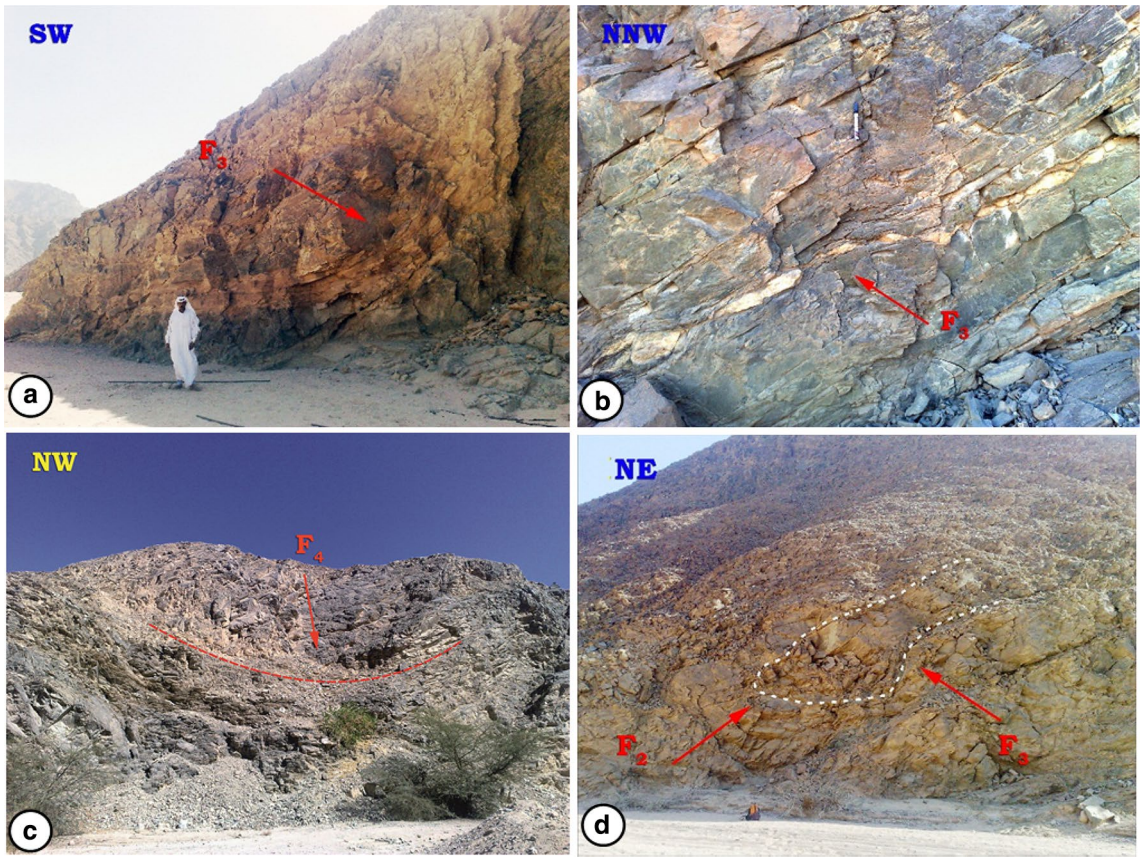

Fig. 23 Field photographs of F_3 and F_4 *open concentric folds* in metasediments **a** F_3 *open concentric fold*, view hight about 10.0 m; **b** F_3 *open concentric fold* of boudinaged quartz, view height about 155 m; **c** F_4 *open concentric fold* located at the entrance of W. Kid, width of view about 45 m; **d** F_2 recumbent *isoclinals fold* refolded by F_3 open concentric fold, width of view about 18 m

recumbent isoclinal folds followed by the development of thrust shear zones that verge mainly due NW and rarely due SE. The early deformational events are characterized by E–W pure coaxial shear of progressive deformation, whereas the shear zones that formed in the later stages of D_2 indicate a simple non-coaxial shear model as mentioned also by Fowler et al. (2010a). D_2 is related to NW–SE compressional stress due to Neoproterozoic collision between east and west Gondwana. F_3 folds are resulted from D_3 and is characterized by the presence of S_3 axial planes. It is characterized by open concentric folds overprinting both F_1 and F_2 formed by flexural slip. The fold hinges plunge to the west-northwest or east-southeast indicate north–northeast–south–southwest shortening. The fourth deformational event D_4 is characterized by NE plunging open concentric folds (F_4) which overprint the pre-existing folds and formed by flexural-slip mechanism during coaxial deformation. It is indicating change in the stress regime as a result of the change in shortening from NE–SW to NW–SE (Fig. 24). This phase probably accompanied with the late stage plutonic emplacement. Shortening during D_4 is probably related to the final assembly between east and west Gondwana (Kröner and Stern 2005). This stage is also characterized by the emplacement of the alkaline suite.

Expression of Najd fault system in northern Arabian–Nubian Shield

The Arabian–Nubian Shield (ANS) forms one of the largest exposures of juvenile continental crust on Earth, comprising ~3×10^6 km^2 (Bentor 1985) (Fig. 25). The Shield was evolved during the Neoproterozoic East African orogeny (900–550 Ma) and is generally viewed as a group of juvenile volcanic arc terranes and ophiolite remnants that were amalgamated during the assembly of the eastern part of Gondwana (Bentor 1985; Stern 1994, 2002; Stein and Goldstein 1996; Jarrar et al. 2003; Meert 2003; Stoeser and Frost 2006).

The Najd fault system (NFS) was first recognized by Brown and Jackson (1960), which is a major transcurrent fault system of Late Proterozoic. It is an NW–SE structure

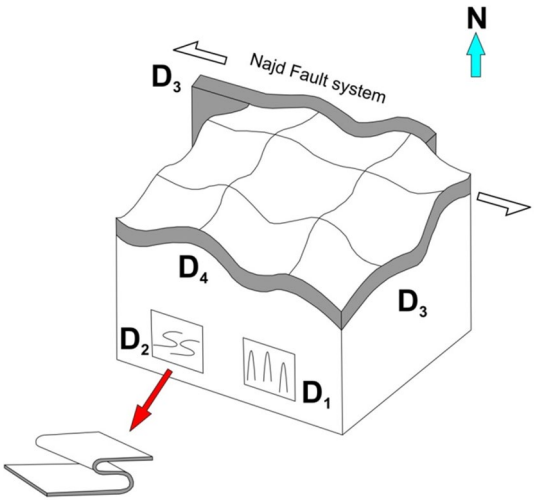

Fig. 24 3D cartoon showing the Najd fault overprints the early folding generations at the Kid metamorphic complex of south Sinai. D_1 is an upright tight to isoclinal large-scale folds that caused few F_1 small-scale folds and a steeply dipping S_1 axial plane foliation. D_2 is characterized by the dominant of sub-horizontal S_2 foliation planes accompanied with recumbent isoclinal folds and NW–SE trending L_2 lineations. F_3 is recorded as an axial plane S_3-surfaces and is characterized by open concentric folding that overprinting both F_1 and F_2 folds; plunging of F_3 fold hinges indicate NNE–SSW shortening during D_3. D_4 is characterized by NE plunging open concentric folding overprint the pre-existing fold generations

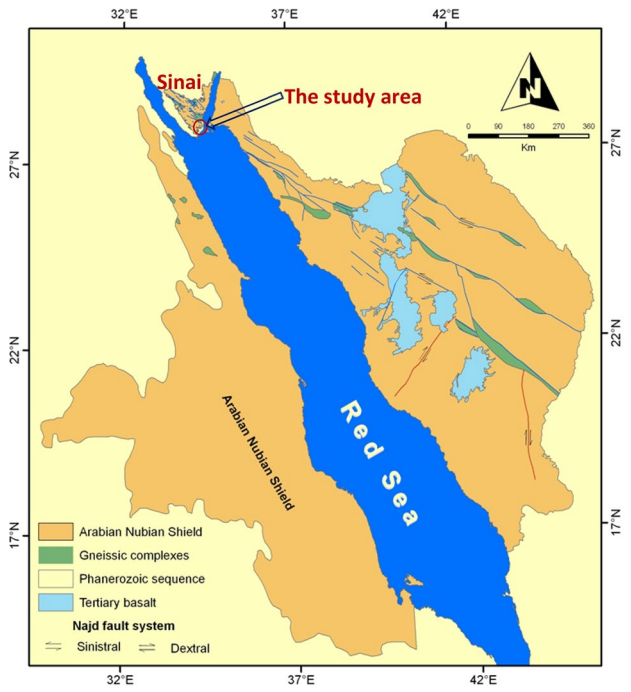

Fig. 25 Metamorphic gneiss complexes, Najd fault system of the northern part of the Arabian–Nubian Shield. (Compiled from Abdelsalam and Stern 1996; Fritz et al. 1996; Johnson 1998; Andresen et al. 2010)

corridor of sinisterly strike-slip faults and plastic shear zone (Brown and Coleman 1972). It is mainly recognized in Saudi Arabia and Egypt. NFS runs through the Precambrian rocks of the ANS and is considered as one of the major longest shear-related structures (1500 km length and about 300 km in width) on Earth. It displays a complete pattern of secondary extensional and compressional structures as an indication of a major transcontinental fault system (McMahon Moore 1979). Deformation style began about 640 Ma ago as a dextral phase of a ductile to brittle regime developed as pull-apart basins (Stacey and Agar 1985; Agar 1986). It started with a dextral sense of shear and changed to sinistral strike-slip system (~620 Ma). A conjugate system with the dominant NW–SE set is probably associated with the NFS (Davies 1984). On the other hand, Abdelsalam (1994) suggested that the NFS formed due to collisional tectonic between east and west Gondwana causing an east–west shortening and the formation of zones of high shear strain in a region inserted between the Nile Craton in the west and the Ar Rayn micro-plate to the east.

Structural elements and the tectonic evolution of Sinai Peninsula (Sultan 2011) is consistent with that of the northern Eastern Desert of Egypt as they exhibit extensional-related tectonic fabric and also intruded by extensive plutonic, volcanic and dike swarms between 800 and 530 Ma (e.g. Bielski 1982; Halpern and Tristan 1981; Kröner et al. 1990, 1994; Moghazi et al. 2012; Eyal et al. 2014). The igneous rock groups in Sinai represent ~70% of the total exposed crystalline rocks. Those are mostly composed of granite with minor occurrences of gabbroic and volcanic rocks. The Granitoids were grouped into two main suites: (1) syn- to late-orogenic I-type and (2) post-orogenic, A-type, the transition between the two types occurred at ~610–600 Ma (Beyth et al. 1994; Stern 1994; Garfunkel 1999; Jarrar et al. 2003; Moussa et al. 2008). On the other hand, the recognition of a widespread high-K calc-alkaline suite, formed at about the time of this transition, and partially overlapping the beginning of alkaline A-type magmatism probably redefines different stages of calc-alkaline magma production in Sinai (Be'eri-Shlevin et al. 2009).

Polyphase deformation associated with compression-related regime is documented within the metamorphic complexes with metamorphic grade range from greenschist to upper amphibolites facies. The metamorphic belts of South Sinai comprise two groups based on structural, metamorphic, compositional and geochronological data: (1) the medium-to-high grade amphibolite faces including the Feiran–Solaf metamorphic complex (FSB) and the Taba metamorphic complex (TB); (2) the low-grade greenschist facies complexes comprising the Sa'al–Zaghra metamorphic complex (SZB) and the Kid metamorphic complex

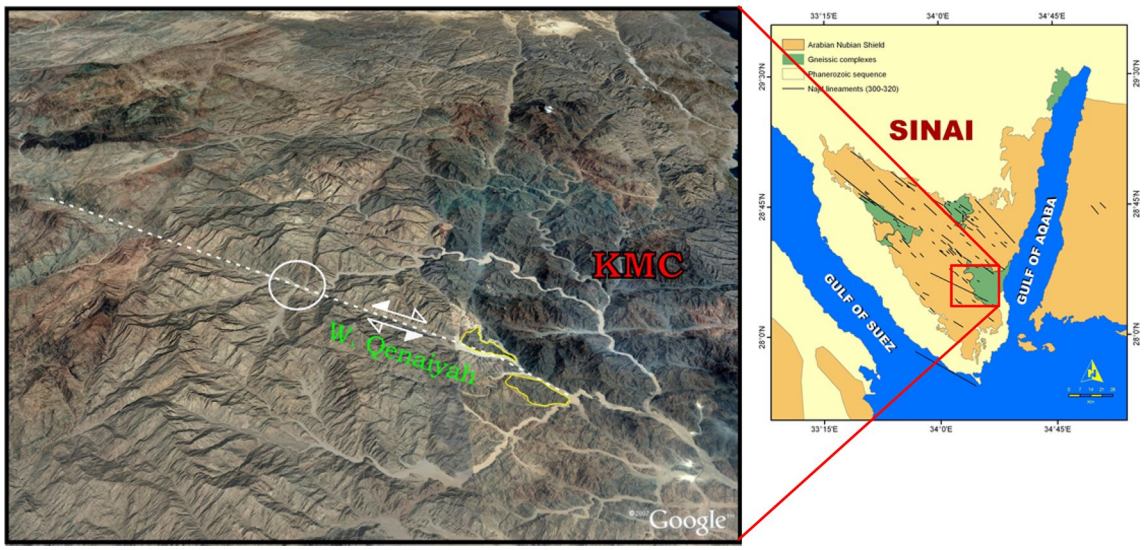

Fig. 26 Google image showing dextral reactivation and the extension of the Najd fault system during Oligo-Miocene along W. Qenaiyah, Kid area of South Sinai

(KMC) (Fig. 1a). Local amphibolite facies rocks are also recognized either at SZB and KMC (El-Shafei et al. 1992; Sultan 2011).

In the KMC, the dextral NW–SE shear zone along W. Qenaiyah that bounded the south western portion of the complex is probably related to reactivation of the NFS during Oligo-Miocene (Fig. 26). The existence of the Dokhan volcanics in South Sinai as noted by Moghazi (2003) and El-Bialy and Ali (2013) also gives a good indication of their eruption during the motivation of NFS. At the Central Eastern desert of Egypt, D_3 deformation is characterized by an overall northwest trending, sinistral transpression regime (Loizenbauer et al. 2001). This event is formed associated with the NFS and the formation and exhumation of the core complexes (Fritz et al. 1996, 2013).

Concluding remarks

Based on both detailed field investigations and image processing analysis carried out during this study, the following concluding remarks are formulated:

1. Kid metamorphic complex is characterized by low-to-medium-grade volcano-sedimentary metamorphic sequence. A complex structure pattern is preserved within the complex as an indicative of long and continuous deformational history.
2. The current study started with applying the modern image processing techniques to discriminate, extract, and mapping the different rock units and structural lineaments. Applying the PCA technique for the ETM^+ 7 images, where PC4, PC3, and PC2 in RGB used to discriminate the different rock units in the investigated complex. Every single rock unit has its own spectral signature and consequently has specific false color that used to distinguish and allocate the geologic contacts.
3. Band ratio combinations 4/2, 5/4, 7/5 in RGB and 5/7, 4/5, 3/1 in RGB are utilized to display different geologic information and depict sharp contrast among various lithologies. In KMC, the band ratio 4/2, 5/4, and 7/5 in RGB has been applied and discriminate among the exposed rock units including metasediments, metavolcanics, metagabbro-diorite complex, granitic orthogneisses, metadiorite, Dokhan volcanics, quartz diorite and gabbro, calc-alkaline granites, and alkaline granite. The metasediments have a pale sky blue to pale green color, whereas the metavolcanics appear in dark blue color, the Dokhan volcanic appears in dark red color, the metadiorite appears in blue color, metagabbro-diorite complex appears in pinkish blue color, granitic orthogneiss appear in greenish yellow color, quartz diorite and gabbro appear in pale blue color, the calc-alkaline appears in yellow to greenish yellow color, and the alkali granite appears in pink color. The discriminated rock units were verified in the field.
4. The present enhanced images discriminate for the first time between the metavolcanis and the metasediments of the northern Kid complex. In addition, ETM^+ 7 are used to differentiate between some granitic bodies and metvolcanic rocks better than ASTER used previously by Gad (2007).

5. In general, the Landsat ETM$^+$ 7 and the IKONOS satellite images are used in the present study to extract detailed structural lineaments such as joints, dikes, and faults. Based on the lineament azimuth frequencies interpreted from the enhanced satellite images, it is concluded that the dominant fracture sets are 30°N–40°E, 40°N–50°E, 20°N–30°W, and 50°N–60°W, respectively. The NE-trending defines the dike swarms that crosscut the surrounding granitoids where the other directions are mostly fault lineament.
6. Structurally, the KMC has reached its present situation through four deformational events (D_1–D_4) (Fowler et al. 2010a, b; Sultan 2011). In the present study, the D_2 and D_3 are dominantly represented, while D_1 and D_4 are rarely recorded in the investigated area. D_1 event is expressed by the compressional tectonic regime and is expressed by upright tight to isoclinal large-scale folds that produced few F_1 small-scale folds and a steeply dipping S_1 axial plane foliation. This phase is thought to have been related to subduction-related island arc between 740 and 870 Ma (Be'eri-Shlevin et al. 2009). The second deformational event D_2 comprises a non-coaxial deformation of the contractional regime and is related to NW–SE compressional thrust tectonics. D_2 is related to the Neoproterozoic collision and accretion of the east and west Gondwana (650–625 Ma, Be'eri-Shlevin et al. 2009). This phase is characterized by S_2 foliations and NW–SE trending L_2 lineations. The main sense of movement was top-to-the-NW and locally directed towards the SE. The third folding generation F_3 is recorded as axial plane S_3-surfaces and is characterized by open concentric folding overprinting both F_1 and F_2 and has a flexural-slip nature. F_3 fold hinges plunge to the west-northwest or east-southeast indicate north–northeast–south–southwest shortening during D_3. The fourth deformational event D_4 is characterized by NE plunging open concentric folding overprint the pre-existing fold generations and formed under flexural slip mechanism reflecting coaxial deformation and indicating a change in the stress regime as a result of the change in shortening from NE–SW to NW–SE. This phase is probably accompanied with the final assembly of east and west Gondwana.
7. The dextral NW–SE shear zone recognized in this study along W. Qenaiyah in the south western portion of the KMC is probably the north-western extension related to the reactivation of the Najd Fault System during Oligo-Miocene in South Sinai.

Acknowledgements Field work was supported by the Suez Canal University, Egypt, which is gratefully acknowledged. The Associate Editor S. Mukherjee and two anonymous reviewers are thanked for offering helpful and constructive comments that improved the paper.

References

Abdelsalam MG (1994) The Oko shear zone: post accretionary deformations in the Arabian-Nubian Shield. J Geol Soc Lond 151:767–776

Abdelsalam MG, Stern RJ (1996) Sutures and shear zones in the Arabian-Nubian Shield. J Afr Earth Sci 23:289–310

Abu El-Enen MM (2008) Geochemistry and metamorphism of the Pan-African back-arc Malhaq Volcano-sedimentary Neoproterozoic association, W. Kid area, SE Sinai, Egypt. J Afr Earth Sci 51(4):189–206

Abu El-Enen MM, Makroum FM (2003) Tectonometamorphic evolution of the northeastern Kid belt, southeast Sinai, Egypt. Ann Geol Surv Egypt 5:19–37

Abu El-Enen MM, Okrusch M, Will TM (2003) Metapelitic assemblages in the Umm Zariq schists, central western Kid Belt, Sinai Peninsula, Egypt. Neues Jahrbuch Mineralogie Abhandlungen 178:277–306

Abu El-Enen MM, Will TM, Okrusch M (2004) P-T evolution of the Taba Metamorphic belt, Egypt: constraints from the metapelitic mineral assemblage assemblages. J Afr Earth Sci 38(1):59–78

Agar RA (1986) The Bani Ghayy group; sedimentation and volcanism in "pull-apart" grabens of the Najd strike-slip orogen, Saudi Arabian Shield. Precambrian Res 31:259–274

Andresen A, Augland LE, Boghdady GY, Lundmark AM, Elnady OM, Hassan, MA (2010) Structural constraints on the evolution of the Meatiq gneiss domes (Egypt), East-African Orogen. J Afr Earth Sci 57:413–422

Arnous MO (2011) Integrated remote sensing and GIS techniques for landslide hazard zonation: a case study Wadi Watier area, South Sinai, Egypt. J Coast Conserv 15(4):477–497

Arnous MO (2016) Groundwater potentiality mapping of hard-rock terrain in arid regions using geospatial modelling: example from Wadi Feiran basin, South Sinai, Egypt. Hydrogeol J 24(6):1375–1392

Arnous MO, Green DR (2011) GIS and remote sensing as tools for conducting geo-hazards risk assessment along Gulf of Aqaba coastal zone, Egypt. J Coast Conserv 15(4):457–475

Arnous MO, Sultan YM (2014) Geospatial technology and structural analysis for geological mapping and tectonic evolution of Feiran–Solaf metamorphic complex, South Sinai, Egypt. Arab J Geosci 7:3023–3049

Be'eri-Shlevin Y, Katzir Y, Valley JW (2009) Crustal evolution and recycling in a juvenile continent: oxygen isotope ratio of zircon in the northern Arabian Nubian Shield. Lithos 107:169–184

Bentor YK (1985) The crustal evolution of the Arabo-Nubian Massive with special reference to the Sinai Peninsula. Precambrian Res 28:1–74

Bentor YK, Eyal M (1987) The geology of southern Sinai; its implication for the evolution of the Arabo-Nubian massif. Jebel Sabbagh Sheet, vol 1. The Israel Academy of Sciences and Humanities, Jerusalem, p 484

Beyth M, Stern RJ, Altherr R, Kroner A (1994) The late Precambrian Timna igneous Complex, southern Israel: evidence for comagmatic-type sanukioid monzodiorite and alkali granite magma. Lithos 31:103–124

Bielski M (1982) Stages of the evolution of the Arabian-Nubian massif in Sinai. Ph.D. thesis. Hebrew University, Jerusalem, p 155

Blasband B, Brooijmans P, Dirks P, Visser W, White S (1997) A Pan-African core complex in the Sinai, Egypt. Geol Mijnbouw 76:247–266

Blasband B, White S, Brooijmans P, De Boorder H, Visser W (2000) Late Proterozoic extensional collapse in the Arabian–Nubian Shield. J Geol Soc Lond 157:615–628

Brooijmans P, Blasband B, White SH, Visser WJ, Dirks P (2003) Geothermobarometric evidence for a metamorphic core complex in Sinai, Egypt. Precambrian Res 123:249–268

Brown GF, Coleman RG (1972) The tectonic framework of the Arabian Peninsula. In: 24th, International Geological Congress 3, 300–305

Brown GF, Jackson RO (1960) The Arabian Shield. In: 21st, International Geological Congress 9, 69–77

Davies FB (1984) Strain analysis of wrench faults and collision tectonics of the Arabian-Nubian Shield. J Geol 92:37–53

El-Bialy MZ (2009) On the Pan-African transition of the Arabian-Nubian shield from compression to extension: the post-collision Dokhan Volcanic suite of Kid-Malhak region, Sinai, Egypt. Gondwana Res 17:26–43

El-Bialy MZ (2010) On the Pan-African transition of the Arabian–Nubian Shield from compression to extension: the post-collision Dokhan volcanic suite of Kid-Malhak region, Sinai, Egypt. Gondwana Res 17(1):26–43

El-Bialy MZ, Ali KA (2013) Zircon trace element geochemical constraints on the evolution of the Ediacaran (600–614 Ma) post-collisional Dokhan Volcanics and Younger Granites of SE Sinai, NE Arabian–Nubian Shield. Chem Geol 360–361:54–73

El-Gaby S, Khudeir AA, Adel Tawab M, Atalla RF (1991) The metamorphosed volcano-sedimentary succession of Wadi Kid, Southeastern Sinai, Egypt. Ann Geol Surv Egypt 16:19–35

Eliwa HA, Abu El-Enen MM, Khalaf I, Itaya T, Murata M (2008) Metamorphic Evolution of Neoproterozoic complexes in the Sinai, Egypt: insights from petrology, mineral chemistry and K-Ar age dating. J Afr Earth Sci 51(3):107–122

El-Metwally AA, El Asay IA, Ibrahim ME, Essawy MA, El Mowafy AA (1999) Petrological, structural and geochemical studies on the basement rocks of Gabal Um Zariq-Wadi Kid area, Southeastern Sinai. Egypt J Geol 43:147–180

El-Shafei MK, Khawasik SM, EI-Ghawaby MA (1992) Deformational styles in the tectonites of Wadi Sa'al, South Sinai. In: Proceedings of the 3rd conference on Geology Sinai Development, Ismailia, Egypt, pp 1–8

Eyal M, Be'eri-Shlevin Y, Eyal Y, Whitehous MJ, Litvinovsky B (2014) Three successive Proterozoic island arcs in the Northern Arabian–Nubian Shield: evidence from SIMS U-Pb dating of zircon. Gondwana Res 25(1):338–351

Fowler A, Hassen IS, Osman AF (2010a) Neoproterozoic structural evolution of SE Sinai, Egypt: I. Re-investigation of the structures and deformation kinematics of the Um Zariq and Malhaq Formations, northern Wadi Kid area. J Afr Earth Sci 58:507–525

Fowler A, Hassen IS, Osman AF (2010b) Neoproterozoic structural evolution of SE Sinai, Egypt: II. Convergent tectonic history of the continental arc Kid Group. J Afr Earth Sci 58:526–546

Fritz H, Wallbrecher E, Khudeir AA, Abu El Ela F, Dallmeyer DR (1996) Formation of Neoproterozoic metamorphic core complexes during oblique convergence (Eastern Desert, Egypt). J Afr Earth Sci 23:311–329

Fritz H, Abdelsalam M, Ali KA, Bingen B, Collins AS, Fowler AR, Ghebreab G, Hauzenberger CA, Johnson PR, Kusky TM, Macey P, Muhongo S, Stern RJ, Viola G (2013) Orogen styles in the East African Orogen: a review of the Neoproterozoic to Cambrian tectonic evolution. J Afr Earth Sci 86:65–106

Furnes H, Shimron AE, Roberts D (1985) Geochemistry of Pan-African volcanic arc sequences in southeastern Sinai Peninsula and plate tectonic implications. Precambrian Res 29:359–382

Gad S (2007) Proterozoic geologic and tectonic evolution of the Wadi Kid Area, Sinai, Egypt, based on field and satellite remote sensing studies. PhD Thesis. St Louis University, USA

Gad S, Kusky T (2006) ASTER spectral rationing for lithological mapping in the Arabian–Nubian Shield, the Proterozoic Wadi Kid area, Sinai, Egypt. Gondwana Res 11:326–335

Garfunkel Z (1999) History and paleogeography during the Pan-African orogen to stable platform transition: reappraisal of the evidence from Elat area and northern Arabian-Nubian Shield. Israel J Earth Sci 48:135–157

Halpern M (1980) Rb-Sr 'Pan-African' isochron ages of Sinai igneous rocks. Geology 8:48–50

Halpern M, Tristan N (1981) Geochronology of the Arabian-Nubian Shield in southern Israel and eastern Sinai. J Geol 89:639–648

Hassanen MA (1992) Geochemistry and petrogenesis of the late Proterozoic Kid volcanics; evidence relevant to arc–intra-arc rifting volcanism in southern Sinai, Egypt. J Afr Earth Sci 14:131–145

Inzana J, Kusky T, Higgs G, Tucker R (2003) Supervised classifications of Landsat TM band ratio images and Landsat TM band ratio image with radar for geological interpretations of central Madagascar. J Afr Earth Sci 37:59–72

Jarrar G, Stern RG, Saffarini H, Al-Zubi (2003) Late- and post-orogenic Neoproterozoic intrusions of Jordan: implications for crustal growth in the northernmost segment of the East African Orogen. Precambrian Res 123:295–319

Johnson PR (1998) Tectonic map of Saudi Arabia and adjacent areas: Saudi Arabian Deputy Ministry for Mineral Resources Technical Report USGS-TR-98-3, scale 1:4,000,000

Koike K, Nagano S, Ohm M (1995) Lineament analysis of satellite images using a segment tracing algorithm (STA). Comput Geosci 21(9):1091–1104

Kröner A, Stern R (2005) AFRICA/Pan-African Orogeny. Encyclopedia of Geology, pp 1–12

Kröner A, Eyal M, Eyal Y (1990) Early Pan-African evolution of the basement around Elat, Israel, and Sinai Peninsula revealed by single-zircon evaporation dating, and implications for crustal accretion rates. Geology 18:545–548

Kröner A, Kruger J, Rashwan, AAA (1994) Age and tectonic setting of granitoid gneisses in the Eastern Desert of Egypt and southwest Sinai. Geol Rundsch 83:502–513

Kusky TM, Ramadan TM (2002) Structural controls on Neoproterozoic mineralisation in the South Eastern Desert, Egypt: an integrated field, Landsat TM, and SIR-C/X SAR approach. J Afr Earth Sci 35:107–121

Loizenbauer J, Wallbrecher E, Fritz H, Neumayr P, Khudeir AA, Kloetzli U (2001) Structural geology, single zircon ages and fluid inclusion studies of the Meatiq metamorphic core complex: implications for Neoproterozoic tectonics in the Eastern Desert of Egypt. Precambrian Res 110:357–383

Mah A, Taylor GR, Lennox P, Balia L (1995) Lineament analysis of Landsat Thematic Mapper Images, Northern Territory, Australia. Photogramm Eng Remote Sens 61:761–773

McMahon Moore J (1979) Tectonics of the Najd Transcurrent Fault System, Saudi Arabia. J Geol Soc Lond 136:441–454

Meert JG (2003) A synopsis of events related to the assembly of eastern Gondwana. Tectonophysics 362:1–40

Moghazi AM (2003) Geochemistry and petrogenesis of a high-K calc-alkaline Dokhan Volcanic suite, South Safaga area, Egypt: the role of late Neoproterozoic crustal extension. Precambrian Res 125:161–178

Moghazi AM, Anderson T, Oweiss GA, El Bouselly AM (1998) Geochemical and Sr–Nd–Pb isotopic data bearing on the origin of Pan-African granitoids in the Kid area, southeast Sinai, Egypt. J Geol Soc Lond 155:697–710

Moghazi AM, Ali K, Wilde SA, Zhou Q, Andersen T, Andersen A, Abu-El Enen M, Stern RJ (2012) Geochemistry, geochronology, and Sr–Nd isotopes of the Late Neoproterozoic Wadi Kid volcano-sedimentary rocks, Southern Sinai, Egypt: implications for tectonic setting and crustal evolution. Lithos 154:147–165

Moussa EMM, Stern RJ, Manton WI, Ali KA (2008) SHRIMP zircon dating and Sm/Nd isotopic investigations of Neoproterozoic granitoids, Eastern Desert, Egypt. Precambrian Res 160:341–356

Mukherjee S (2010a) Microstructures of the Zanskar Shear Zone. Earth Sci India 3:9–27
Mukherjee S (2010b) Structures in Meso- and Micro-scales in the Sutlej section of the Higher Himalayan Shear Zone, Indian Himalaya. e-Terra 7:1–27
Mukherjee S (2013a) Higher Himalaya in the Bhagirathi section (NW Himalaya, India): its structures, backthrusts and extrusion mechanism by both channel flow and critical taper mechanisms. Int J Earth Sci (Geol Rundsch) 102:1851–1870
Mukherjee S, (2013b) Deformation Microstructures in Rocks. Springer Geochemistry/Mineralogy, Berlin, pp 1–111
Mukherjee S (2014a) Atlas of Shear Zone Structures in Meso-scale. Springer Geology, Cham, pp 1–124
Mukherjee S (2014b) Review of flanking structures in meso- and micro-scales. Geol Mag 151:957–974
Mukherjee S (2015) Atlas of structural geology. Elsevier, Amsterdam
Mukherjee S (2016) Review on symmetric structures in ductile shear zones. Int J Earth Sci (Geol Rundsch). doi:10.1007/s00531-016-1366-4
Mukherjee S, Koyi HA (2010a) Higher Himalayan Shear Zone, Sutlej section—structural geology and extrusion mechanism by various combinations of simple shear, pure shear and channel flow in shifting modes. Int J Earth Sci (Geol Rundsch) 99:1267–1303
Mukherjee S, Koyi HA (2010b) Higher Himalayan Shear Zone, Zanskar section—microstructural studies and extrusion mechanism by a combination of simple shear and channel flow. Int J Earth Sci (Geol Rundsch) 99:1083–1110
Mukherjee S, Punekar J, Mahadani T, Mukherjee R (2015) A review on intrafolial folds and their morphologies from the detachments of the western Indian Higher Himalaya. In: Mukherjee S, Mulchrone KF (Eds.) Ductile Shear Zones: From Micro- to Macro-scales. Wiley, Hoboken, pp. 182–205.
Navon O, Reymer APS (1984) Stratigraphy, structure and metamorphism of Pan-African age in Central Wadi Kid, Southeastern Sinai. Isr J Earth Sci 33:135–149
Novak ID, Soulakellis N (2000) Identifying geomorphic features using landsat-5/TM data processing techniques on Lesvos, Greece. Geomorphology 34(7):101–109
Passchier CW, Trouw RA (1996) Micro-tectonics. Springer, Berlin, p 282
Reymer APS, Oertel G (1985) Horizontal cleavage in southeastern Sinai: the case for a coaxial strain history. J Struct Geol 7:623–636
Reymer APS, Yogev A (1983) Stratigraphy and tectonic history of the Southern Wadi Kid metamorphic complex, Southeastern Sinai. Israel J Earth Sci 32:105–116
Reymer APS, Matthews A, Navon O (1984) Pressure–temperature conditions in the Wadi Kid metamorphic complex: implications for the Pan-African event in SE Sinai. Contrib Mineral Petrol 85:336–345
Shalaby A, Shawky M (2014) Morphotectonics of Kid drainage basin, Southeastern Sinai: a landscape evolution coeval to Gulf of Aqaba-Dead Sea rifting. J Afr Earth Sci 100:289–302
Shimron AE (1980) Proterozoic island arc volcanism and sedimentation in Sinai. Precambrian Res 12:437–458
Shimron AE (1983) The Tarr Complex revisited-folding, thrusts, and mélange in the Southern Wadi Kid region, Sinai Peninsula. Israel J Earth Sci 32:123–148
Shimron AE (1984a) Evolution of the Kid Group, Southeastern Sinai Peninsula: thrusts, mélange, and implications for accretionary tectonics during the Late Proterozoic of the Arabian-Nubian Shield. Geology 12:242–247
Shimron AE (1984b) Metamorphism and tectonics of a Pan-African terrain in southeastern Sinai-a discussion. Precambrian Res 24:189–197
Stacey JS, Agar R A (1985) U-Pb isotopic evidence for the accretion of a continental microplate in the Zalm region of the Saudi Arabian Shield. J Geol Soc Lond 142:1189–1204
Stein M, Goldstein S (1996) From plume head to continental lithosphere in the Arabian-Nubian Shield. Nature 382:773–778
Stern RJ (1994) Arc assembly and continental collision in the Neoproterozoic East African Orogen: implications for the consolidation of Gondwanaland. Annu Rev Earth Planet Sci 22:319–351
Stern RJ (2002) Crustal evolution in the East African Orogen: a neodymium isotopic perspective. J Afr Earth Sci 34:109–117
Stern RJ, Manton WI (1987) Age of Feiran basement rocks, Sinai: implications for late Precambrian crustal evolution in the northern Arabian-Nubian Shield. Geol Soc Lond J 144:569–575
Stoeser DB, Frost CD (2006) Nd, Pb, Sr, and O isotopic characterization of Saudi Arabian Shield terranes. Chem Geol 226:163–188
Sultan YM (2011) Tectonic setting of South Sinai metamorphic belts based on remote sensing, structural analysis and GIS. Ph.D. thesis, Suez Canal University, Faculty of Science, Geology Depart, Ismailia, p 225
Sultan M, Arvidson RE, Sturchio NC (1987a) Reply—Mapping of serpentinites in the Eastern Desert of Egypt using Landsat Thematic Mapper. Geology 874–875
Sultan M, Arvidson RE, Sturchio NC, Guinness E (1987b) Lithologic mapping in arid regions with Landsat Thematic Mapper data: Meatiq Dome, Egypt. Geol Soc Am Bull 99:748–762
Süzen ML, Toprak V (1998) Filtering of satellite images in geological lineament analyses: an application to a fault zone in Central Turkey. Int J Remote Sens 19(19):1101–1114